Received: Added at production | Revised: Added at production | Accepted: Added at production

DOI: xxx/xxxx

RESEARCH ARTICLE-APPLICATION

Computational modeling of the kidney hemodynamics with a coupled unsteady Stokes-Darcy model

Fenfen Qi[1] | Yingzhi Liu[1] | Rongliang Chen[2] | Pengzhi Hu[3] | Xiao-Chuan Cai*[4]

[1]Department of Mathematics, University of Macau, Macau, China
[2]Shenzhen Institutes of Advanced Technology, Chinese Academy of Sciences, Shenzhen, China
[3]The Third Xiangya Hospital of Central South University, Changsha, China
[4]Department of Mathematics, University of Macau, Macau, China

Correspondence
*Xiao-Chuan Cai, Department of Mathematics, University of Macau, Macau, China.
Email: xccai@um.edu.mo

Summary

We consider the numerical simulation of blood flows in a patient-specific kidney including the renal artery, the renal vein, and the kidney tissue using a coupled system of unsteady Stokes-Darcy equations. The Stokes equations and the Darcy equations are implicitly coupled on the interfaces by enforcing three conditions, namely the conservation of mass, the balance of the normal force and the Beavers-Joseph-Saffman condition. To discretize the system we introduce a stabilized P1-P1-P1 finite element method for the spatial variables and an implicit backward Euler method for the temporal variable. A mathematical theory is developed to guarantee the stability and the convergence of the proposed discretization method. To efficiently solve the large, sparse and highly ill-conditioned algebraic systems, we further propose a Krylov subspace method preconditioned by a robust two-scale additive Schwarz method consisting of a mixed-dimensional coarse preconditioner with a 1D centralline preconditioner in the vascular region and a 3D preconditioner for the kidney tissue with some compatibility conditions imposed on the 1D and 3D interfaces. Some numerical experiments for a benchmark problem and a patient-specific kidney with physiologic parameters are presented to verify the accuracy, the robustness, and the effectiveness of the proposed method.

KEYWORDS:
Patient-specific kidney, blood flow and tissue, coupled unsteady Stokes-Darcy equations, two-scale Schwarz preconditioner, fully implicit finite element method

1 | INTRODUCTION

The kidney is a vital organ in the abdominal cavity responsible for filtering the oxygenated blood from the renal artery to produce urine and then the deoxygenated blood is carried away from the kidney by the renal vein, returning back to the heart for further circulation. Several diseases may reduce kidney function such as renal artery stenosis and aneurysm. While the diagnosis of these diseases is often through the use of computed tomography (CT) and magnetic resonance imaging (MRI), the renal arteriography is considered as the gold standard, more recently some hemodynamic indexes such as the renal fractional flow reserve (rFFR) [1] have been employed to quantitatively evaluate the risk status of the stenosis. In this paper, we develop an image-based numerical method for the simulation of a patient-specific kidney, and more precisely, for the analysis of the behavior of blood flows and for the prediction of certain renovascular or kidney diseases. To model the hemodynamics of the kidney, we propose a method that combines a fluid with a porous medium model, more specifically, the process involves the following steps: (1) a patient-specific renal vessel geometry is segmented from the CT images and a blood flow model is built with the incompressible Stokes

equations with several patient-specific inflow and outflow conditions; (2) the geometry of the kidney tissue is segmented from the CT images, and to model the microvascular structure of the kidney with a rich capillary network, we employ the Darcy equations and treat the microvascular bed that can not be resolved by the CT as a porous medium; (3) for the coupling between the fluid and the porous medium models, we impose three interface conditions based on the conservation of mass, the balance of the normal force and the Beavers-Josepha-Saffman (BJS) condition[2]. We note that the interface region is typically composed of the distal sections of blood vessels that can be segmented from the images and smaller vessels that can not be segmented from the images but are attached to the wall of the larger vessels. To model the situation, the blood flow is allowed to penetrate from the wall into the kidney tissue. The coupled system approach provides higher physical fidelity than either the Stokes or the Darcy model on its own and therefore is widely used in other important applications such as groundwater systems[3], industrial filtrations[4] and petroleum extraction[5].

There are many works in patient-specific numerical simulations of blood flows in, for example, the abdominal aorta[6], the cerebral artery[7] and the cardiovascular systems[8]. Concerning the renal networks, Taylor et al.[9] simulated a pulsatile flow in a hypothetical abdominal aorta with two tube-like renal arteries. For the patient-specific abdominal aorta including the major renal arteries, Berg et al.[10] studied the effect of the stenosis on the blood flow. In[11], the renal vascular network is simplified to some connected straight pipes in which the blood flows are computed. In[12], Bortolussi adopted a coupled one-dimensional (1D) fluid model in the renal artery and a three-dimensional (3D) Darcy model in a box region to model the flow in the kidney. All the aforementioned works assume some simplified geometries. In this paper, we focus on a 3D coupled unsteady Stokes-Darcy model for the blood flow in the patient-specific renal artery and vein (the fluid domain), and the kidney tissue (the porous medium domain), and study the basic formulation of the coupled method including its discretization, stability and convergence properties, and as an application, we compute the hemodynamics of a patient-specific kidney. We mention that such combined fluid and porous medium methods have been applied to other problems, for example, the simulation of fractured reservoir[13], the simulation of human liver[14,15] as well as the simulation of myocardia[16].

There are many existing techniques for the discretization of the Stokes-Darcy system such as finite element methods[17,18,19,20], Lagrange multiplier methods[21,22,23,24,25], discontinuous Galerkin methods[26,27] and boundary integral methods[28]. There are also several classes of algebraic solvers for the discretized systems such as multigrid methods[29] and non-overlapping domain decomposition methods (DDMs)[30,31,32,33,34]. All the solvers decouple the system into a fluid subproblem and a porous medium subproblem and solve them iteratively in each subdomain. The decoupled approaches are easy to implement, but the major difficulties are how to update the interface conditions and choose optimal interface parameters[35,36] to guarantee the convergence, especially for interfaces involving complex geometries and models with many parameters.

In this paper, we propose a multi-physics model for simulations of blood flows in a patient-specific kidney, in which we couple the blood flow problem in the vessels described by the Stokes equations with patient-specific wall/inlet/outlet conditions and the blood flow in the kidney tissue modeled by the Darcy equations through three interface conditions. We adopt the primal formulation of the Darcy equation to weakly impose the continuity condition of the normal components of the fluid velocity across the interface, avoiding the introduction of Lagrange multipliers[18,26]. In order to circumvent the inf-sup condition, a P1-P1-P1 finite element method with stabilization terms is employed to discretize our model problem. To establish the stability and convergence theory of the proposed finite element method, it is crucial to introduce a parameter dependent L^2-norm of the pressure in the Stokes equations to deal with the interface and boundary conditions, which is different from the analysis of the Stokes equations with the Dirichlet boundary condition[37,38]. Based on this norm, we prove the stability and convergence based on a parameter dependent energy norm and techniques introduced for the Brinkman model[39]. Moreover, we introduce and study an efficient and robust two-level overlapping additive Schwarz preconditioner with a novel mixed-dimensional coarse preconditioner consisting of a one-dimensional central-line coarse preconditioner in the vascular region and a three-dimensional coarse preconditioner for the kidney tissue, which extends the central-line method, originally developed for blood flow problems in arteries[45,44] to multi-physics hemodynamic problems. An important component of the two-level method is a special interpolation framework for the construction of the coarse space, and also for the construction of the extension and restriction matrices with different coarse basis functions for different fields such as conical basis functions for the velocity and radial basis functions for the pressure field in the kidney tissue. The theoretical results and the performance of the proposed preconditioner are verified by some numerical experiments with simplified and realistic settings including geometries and parameters.

The rest of the paper is organized as follows. In Section 2, we describe the coupled unsteady Stokes-Darcy model, the existence and uniqueness of the weak solution and the stabilized finite element discretization. Section 3 focuses on the stability and convergence analysis. A two-level additive Schwarz preconditioner with a 1D-3D coarse preconditioner is proposed in Section

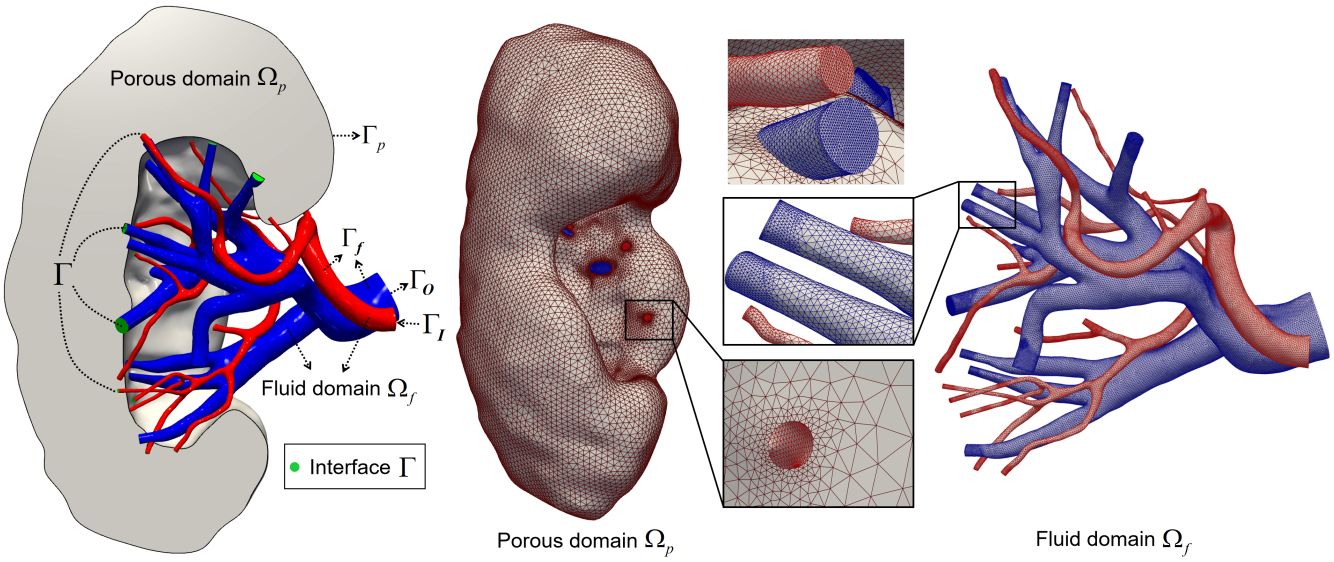

Figure 1 A schematic of the patient-specific domain consisting of the renal artery in red, the renal vein in blue, and the kidney tissue in gray; and unstructured tetrahedral meshes in the vessels and the kidney tissue, which are matched on the interface.

4. Some numerical experiments are presented to confirm the theoretical order of convergence and show the effectiveness of the proposed method in Section 5. Finally, we draw some conclusions in Section 6.

2 | COUPLED UNSTEADY STOKES-DARCY MODEL AND ITS STABILIZED FINITE ELEMENT DISCRETIZATION

Consider a patient-specific kidney denoted as Ω shown in Fig. 1, including the renal artery (red) and the vein (blue) as the fluid domain Ω_f, and the kidney tissue (light red) as the porous medium domain Ω_p. These two domains are separated by the interface Γ. To simulate the behavior of blood flows in the kidney, we consider the coupled unsteady Stokes-Darcy equations. Specifically, for the flow in the fluid domain Ω_f, we introduce the unsteady incompressible Stokes equations

$$\begin{cases} \rho\dfrac{\partial \boldsymbol{u}_f}{\partial t} - \nabla\cdot\mathbb{T}(\boldsymbol{u}_f, p_f) = \boldsymbol{f}_f, & \text{in } \Omega_f\times(0,T], \\ \nabla\cdot\boldsymbol{u}_f = 0, & \text{in } \Omega_f\times(0,T], \\ \boldsymbol{u}_f(x,0) = \boldsymbol{u}_0(x), & \text{in } \Omega_f, \end{cases} \tag{1}$$

where $\boldsymbol{u}_f$ and p_f are the blood velocity and pressure in the vessels, respectively, ρ is the blood density, μ is the kinematic viscosity of the blood, $\boldsymbol{f}_f$ is the given source term, $\boldsymbol{u}_0$ is the initial velocity, $\mathbb{T}(\boldsymbol{u}_f, p_f) = 2\mu\mathbb{D}(\boldsymbol{u}_f) - p_f\mathbb{I}$ is the stress tensor, $\mathbb{D}(\boldsymbol{u}_f) = \frac{1}{2}(\nabla\boldsymbol{u}_f + \nabla^T\boldsymbol{u}_f)$ is the deformation tensor and $\mathbb{I}$ is the identity tensor; for the porous medium domain Ω_p, it is governed by the Darcy equations

$$\begin{cases} S_0\dfrac{\partial p_p}{\partial t} - \nabla\cdot(\mathbb{K}\nabla p_p) = f_p, & \text{in } \Omega_p\times(0,T], \\ p_p(x,0) = p_{p,0}(x), & \text{in } \Omega_p, \end{cases} \tag{2}$$

where p_p is the Darcy pressure in the porous medium domain, $p_{p,0}$ is the given initial pressure, S_0 denotes the mass storativity coefficient and $\mathbb{K}$ represents the permeability tensor. Here we assume that $\mathbb{K}$ is symmetric and positive definite. The Stokes and Darcy models are coupled by the following three conditions on the interface Γ

$$\boldsymbol{u}_f\cdot\boldsymbol{n}_f = (\mathbb{K}\nabla p_p)\cdot\boldsymbol{n}_p, \tag{3}$$

$$-\boldsymbol{n}_f\cdot(\mathbb{T}(\boldsymbol{u}_f, p_f)\cdot\boldsymbol{n}_f) = p_p, \tag{4}$$

$$-\boldsymbol{\tau}_i\cdot(\mathbb{T}(\boldsymbol{u}_f, p_f)\cdot\boldsymbol{n}_f) = \alpha\boldsymbol{\tau}_i\cdot\boldsymbol{u}_f,\ (i=1,2), \tag{5}$$

where $\boldsymbol{n}_f$ and $\boldsymbol{n}_p$ denote the unit outward normal vectors to the free flow region and the porous medium region, respectively, particularly $\boldsymbol{n}_f = -\boldsymbol{n}_p$ on the interface, $\boldsymbol{\tau}_i$ denotes unit tangential vectors to the interface and α is a parameter in the BJS condition (5).

Denote Γ_I as the inlet of the artery, Γ_O the outlet of the vein, $\Gamma_f = \partial\Omega_f \setminus (\Gamma \cup \Gamma_I \cup \Gamma_O)$ the wall of the artery and vein, and $\Gamma_p = \partial\Omega_p \setminus \Gamma$ the wall of the kidney. On the boundaries, we impose the following boundary conditions

$$\begin{aligned} \boldsymbol{u}_f &= \boldsymbol{u}_I, && \text{on } \Gamma_I \times (0,T], \\ \boldsymbol{u}_f &= \boldsymbol{0}, && \text{on } \Gamma_f \times (0,T], \\ -\mathbb{T}(\boldsymbol{u}_f, p_f)\cdot \boldsymbol{n}_f &= p_O \cdot \boldsymbol{n}_f, && \text{on } \Gamma_O \times (0,T], \\ -\mathbb{K}\nabla p_p \cdot \boldsymbol{n}_p &= 0, && \text{on } \Gamma_p \times (0,T], \end{aligned} \tag{6}$$

where $\boldsymbol{u}_I$ is the inlet velocity and p_O is the outlet pressure.

Now, we define the following Sobolev spaces

$$\begin{aligned} &\boldsymbol{V}_f = \{\boldsymbol{v}_f \in \boldsymbol{H}^1(\Omega_f) : \boldsymbol{v}_f|_{\Gamma_I} = \boldsymbol{u}_I, \boldsymbol{v}_f|_{\Gamma_f} = 0\}, \\ &\boldsymbol{V}_f^0 = \{\boldsymbol{v}_f \in \boldsymbol{H}^1(\Omega_f) : \boldsymbol{v}_f|_{\Gamma_I \cup \Gamma_f} = 0\}, \\ &W_f = L^2(\Omega_f), \quad W_p = H^1(\Omega_p), \end{aligned}$$

and denote $(u,v)_D = \int_D uv$ as the inner product and $\|u\|_{k,D}$ the $H^k(D)$ norm of u, then the variational formulation of the coupled Stokes-Darcy system (1)–(6) is to find $\boldsymbol{u}_f(t) \in \boldsymbol{V}_f$, $p_f(t) \in W_f$, $p_p(t) \in W_p$, such that

$$\begin{aligned} &\left(\rho\frac{\partial \boldsymbol{u}_f}{\partial t}, \boldsymbol{v}_f\right)_{\Omega_f} + \left(S_0\frac{\partial p_p}{\partial t}, q_p\right)_{\Omega_p} + a([\boldsymbol{u}_f, p_p], [\boldsymbol{v}_f, q_p]) + b(\boldsymbol{v}_f, p_f) - b(\boldsymbol{u}_f, q_f) \\ &= \left(\boldsymbol{f}_f, \boldsymbol{v}_f\right)_{\Omega_f} + \left(f_p, q_p\right)_{\Omega_p} - \left(p_O, \boldsymbol{v}_f \cdot \boldsymbol{n}_f\right)_{\Gamma_O}, \ \forall\, \boldsymbol{v}_f \in \boldsymbol{V}_f^0,\ q_f \in W_f,\ q_p \in W_p, \\ &\boldsymbol{u}_f(x,0) = \boldsymbol{u}_0(x), \quad p_p(x,0) = p_{p,0}(x), \end{aligned} \tag{7}$$

for all $t \in (0,T]$, where

$$\begin{aligned} a([\boldsymbol{u}_f, p_p], [\boldsymbol{v}_f, q_p]) &= \left(2\mu\mathbb{D}(\boldsymbol{u}_f), \mathbb{D}(\boldsymbol{v}_f)\right)_{\Omega_f} + \alpha\sum_{i=1}^{2}\left(\boldsymbol{\tau}_i\cdot\boldsymbol{u}_f, \boldsymbol{\tau}_i\cdot\boldsymbol{v}_f\right)_{\Gamma} \\ &\quad + \left(\mathbb{K}\nabla p_p, \nabla q_p\right)_{\Omega_p} + \left(p_p, \boldsymbol{v}_f\cdot\boldsymbol{n}_f\right)_{\Gamma} - \left(\boldsymbol{u}_f\cdot\boldsymbol{n}_f, q_p\right)_{\Gamma}, \\ b(\boldsymbol{u}_f, q_f) &= -\left(q_f, \nabla\cdot\boldsymbol{u}_f\right)_{\Omega_f}. \end{aligned}$$

In the following, C denotes a positive constant independent of μ, $\mathbb{K}$ and also the mesh size h and the time step size Δt when addressing the following discretized problem. The value of C may be different at different inequalities and we use the notation $x \lesssim y$ ($x \gtrsim y$) to represent $x \leqslant Cy$ ($x \geqslant Cy$). Define the norm of $V_f^0 \times W_p$ by $\left(\|\boldsymbol{u}_f\|_{1,\Omega_f}^2 + \|p_p\|_{1,\Omega_p}^2\right)^{\frac{1}{2}}$. Using the Korn's inequality[40], we get the Gårding-type inequality of $a(\cdot,\cdot)$

$$\begin{aligned} a([\boldsymbol{u}_f, p_p], [\boldsymbol{u}_f, p_p]) &= \left(2\mu\mathbb{D}(\boldsymbol{u}_f), \mathbb{D}(\boldsymbol{u}_f)\right)_{\Omega_f} + \alpha\sum_{i=1}^{2}\left(\boldsymbol{\tau}_i\cdot\boldsymbol{u}_f, \boldsymbol{\tau}_i\cdot\boldsymbol{u}_f\right)_{\Gamma} + \left(\mathbb{K}\nabla p_p, \nabla p_p\right)_{\Omega_p} \\ &\geqslant 2\mu\|\mathbb{D}(\boldsymbol{u}_f)\|_{0,\Omega_f}^2 + \lambda_{\min}(\mathbb{K})\|\nabla p_p\|_{0,\Omega_p}^2 + \alpha\sum_{i=1}^{2}\|\boldsymbol{\tau}_i\cdot\boldsymbol{u}_f\|_{0,\Gamma}^2 \\ &\geqslant C\left(\left[\mu\|\boldsymbol{u}_f\|_{1,\Omega_f}^2 + \lambda_{\min}(\mathbb{K})\|p_p\|_{1,\Omega_p}^2\right] - \left[\mu\|\boldsymbol{u}_f\|_{0,\Omega_f}^2 + \lambda_{\min}(\mathbb{K})\|p_p\|_{0,\Omega_p}^2\right]\right), \end{aligned}$$

where $\lambda_{\min}(\mathbb{K})$ is the smallest eigenvalue of $\mathbb{K}$. Using the trace theorem, we obtain the continuity of $a(\cdot,\cdot)$

$$\begin{aligned} a([\boldsymbol{u}_f, p_p], [\boldsymbol{v}_f, q_p]) \leqslant& 2\mu\|\mathbb{D}(\boldsymbol{u}_f)\|_{0,\Omega_f}\cdot\|\mathbb{D}(\boldsymbol{v}_f)\|_{0,\Omega_f} + \alpha\sum_{i=1}^{2}\|\boldsymbol{\tau}_i\cdot\boldsymbol{u}_f\|_{0,\Gamma}\cdot\|\boldsymbol{\tau}_i\cdot\boldsymbol{v}_f\|_{0,\Gamma} \\ &+ \lambda_{\max}(\mathbb{K})\|\nabla p_p\|_{0,\Omega_p}\cdot\|\nabla q_p\|_{0,\Omega_p} + \|p_p\|_{0,\Gamma}\cdot\|\boldsymbol{v}_f\cdot\boldsymbol{n}_f\|_{0,\Gamma} + \|\boldsymbol{u}_f\cdot\boldsymbol{n}_f\|_{0,\Gamma}\cdot\|q_p\|_{0,\Gamma} \\ \leqslant& C\left(\mu\|\boldsymbol{u}_f\|_{1,\Omega_f}^2 + \lambda_{\max}(\mathbb{K})\|p_p\|_{1,\Omega_p}^2\right)^{1/2}\left(\mu\|\boldsymbol{v}_f\|_{1,\Omega_f}^2 + \lambda_{\max}(\mathbb{K})\|q_p\|_{1,\Omega_p}^2\right)^{1/2}, \end{aligned}$$

where $\lambda_{\max}(\mathbb{K})$ is the largest eigenvalue of $\mathbb{K}$. Combining the Gårding-type inequality and continuity of $a(\cdot,\cdot)$ and the inf-sup condition[41] of $b(\cdot,\cdot)$, (7) has a unique weak solution[19].

To discretize (7), we generate a shape-regular unstructured tetrahedral mesh $\mathcal{T}_h$ in Ω consisting of a tetrahedral mesh $\mathcal{T}_h^f$ in Ω_f and $\mathcal{T}_h^p$ in Ω_p which are matched on the interface, see Fig. 1. Denote S_h^f and S_h^p as the continuous, piecewise linear polynomial function spaces on $\mathcal{T}_h^f$ and $\mathcal{T}_h^p$, respectively. Define the finite element spaces

$$\boldsymbol{V}_{f,h} = \left[S_h^f\right]^3 \cap \boldsymbol{V}_f,\ \boldsymbol{V}_{f,h}^0 = \left[S_h^f\right]^3 \cap \boldsymbol{V}_f^0$$

for the velocity and

$$W_{f,h} = S_h^f \cap W_f,\ W_{p,h} = S_h^p \cap W_p$$

for the pressures. Taking advantages of the low- and equal-order finite element pair in terms of the computational complexity and the ease of implementation compared with the stable finite element pairs, following[38], we use a stabilized finite element method spatially and the implicit backward Euler method temporally with the fixed time step size Δt to discretize the weak formulation (7), that is to find $\boldsymbol{u}_{f,h}^n \in \boldsymbol{V}_{f,h}$, $p_{f,h}^n \in W_{f,h}$, $p_{p,h}^n \in W_{p,h}$ at each time step $t^n = n\Delta t$, such that

$$\begin{aligned}
&\left(\frac{\rho}{\Delta t}\boldsymbol{u}_{f,h}^n, \boldsymbol{v}_{f,h}\right)_{\Omega_f} + \left(\frac{S_0}{\Delta t}p_{p,h}^n, q_{p,h}\right)_{\Omega_p} + a([\boldsymbol{u}_{f,h}^n, p_{p,h}], [\boldsymbol{v}_{f,h}, q_{p,h}]) + b(\boldsymbol{v}_{f,h}, p_{f,h}^n) - b(\boldsymbol{u}_{f,h}^n, q_{f,h}) \\
&+\beta \sum_{K\in\mathcal{T}_h^f} h_K^2 \frac{\rho}{\Delta t}\left(\boldsymbol{u}_{f,h}^n, \nabla q_{f,h}\right)_K + \beta \sum_{K\in\mathcal{T}_h^f} h_K^2(\nabla p_{f,h}^n, \nabla q_{f,h})_K \\
&= \left(\frac{\rho}{\Delta t}\boldsymbol{u}_{f,h}^{n-1}, \boldsymbol{v}_{f,h}\right)_{\Omega_f} + \left(\frac{S_0}{\Delta t}p_{p,h}^{n-1}, q_{p,h}\right)_{\Omega_p} + \left(\boldsymbol{f}_f, \boldsymbol{v}_{f,h}\right)_{\Omega_f} + \left(f_p, q_{p,h}\right)_{\Omega_p} - \left(p_O, \boldsymbol{v}_{f,h}\cdot\boldsymbol{n}_f\right)_{\Gamma_O} \\
&+\beta \sum_{K\in\mathcal{T}_h^f} h_K^2(\boldsymbol{f}_f, \nabla q_{f,h})_K + \beta \sum_{K\in\mathcal{T}_h^f} h_K^2 \frac{\rho}{\Delta t}\left(\boldsymbol{u}_{f,h}^{n-1}, \nabla q_{f,h}\right)_K,
\end{aligned} \tag{8}$$

for all $\boldsymbol{v}_{f,h} \in \boldsymbol{V}_{f,h}^0$, $q_{f,h} \in W_{f,h}$, $q_{p,h} \in W_{p,h}$. Here β is a stabilization parameter and h_K is the diameter of element K. Let $\boldsymbol{U}_f^n$, $\boldsymbol{P}_f^n$ and $\boldsymbol{P}_p^n$ be the unknown vectors of $\boldsymbol{u}_{f,h}^n$, $p_{f,h}^n$ and $p_{p,h}^n$, respectively. Then the matrix form can be written as

$$\begin{pmatrix} \frac{1}{\Delta t}\boldsymbol{M}_1 + \boldsymbol{A} + \boldsymbol{I}_1 & \boldsymbol{B}^T & \boldsymbol{I}_2^T \\ -\boldsymbol{B} + \frac{1}{\Delta t}\boldsymbol{S}_1 & S_2 & 0 \\ -\boldsymbol{I}_2 & 0 & \frac{1}{\Delta t}M_2 + D \end{pmatrix} \begin{pmatrix} \boldsymbol{U}_f^n \\ \boldsymbol{P}_f^n \\ \boldsymbol{P}_p^n \end{pmatrix} = \begin{pmatrix} \boldsymbol{F}_{f1} + \frac{1}{\Delta t}\boldsymbol{M}_1\boldsymbol{U}_f^{n-1} \\ F_{f2} + \frac{1}{\Delta t}\boldsymbol{S}_1\boldsymbol{U}_f^{n-1} \\ F_p + \frac{1}{\Delta t}M_2\boldsymbol{P}_p^{n-1} \end{pmatrix}, \tag{9}$$

where the submatrices on the left-hand side satisfy

$$\begin{aligned}
&\boldsymbol{M}_{1,ij} = \rho\left(\boldsymbol{\Phi}_{j,f}, \boldsymbol{\Phi}_{i,f}\right)_{\Omega_f},\ \boldsymbol{A}_{ij} = 2\mu\left(\mathbb{D}(\boldsymbol{\Phi}_{j,f}), \mathbb{D}(\boldsymbol{\Phi}_{i,f})\right)_{\Omega_f},\quad \boldsymbol{I}_{1,ij} = \alpha\sum_{k=1}^{2}\left(\boldsymbol{\tau}_k\cdot\boldsymbol{\Phi}_{j,f}, \boldsymbol{\tau}_k\cdot\boldsymbol{\Phi}_{i,f}\right)_\Gamma, \\
&\boldsymbol{B}_{ij} = \left(\nabla\cdot\boldsymbol{\Phi}_{j,f}, \phi_{i,f}\right)_{\Omega_f},\ \boldsymbol{S}_{1,ij} = \beta\rho\sum_{K\in\mathcal{T}_h^f} h_K^2\left(\boldsymbol{\Phi}_{j,f}, \nabla\phi_{i,f}\right)_K,\ S_{2,ij} = \beta\sum_{K\in\mathcal{T}_h^f} h_K^2(\nabla\phi_{j,f}, \nabla\phi_{i,f})_K, \\
&\boldsymbol{I}_{2,ij} = \left(\boldsymbol{\Phi}_{j,f}\cdot\boldsymbol{n}_f, \phi_{i,p}\right)_\Gamma,\ M_{2,ij} = S_0\left(\phi_{j,p}, \phi_{i,p}\right)_{\Omega_p},\quad D_{ij} = \left(\mathbb{K}\nabla\phi_{j,p}, \nabla\phi_{i,p}\right)_{\Omega_p},
\end{aligned}$$

and the vectors in the right-hand side are given by

$$\boldsymbol{F}_{f1,i} = \left(\boldsymbol{f}_f, \boldsymbol{\Phi}_{i,f}\right)_{\Omega_f} - \left(p_O, \boldsymbol{\Phi}_{i,f}\cdot\boldsymbol{n}_f\right)_{\Gamma_O},\ F_{f2,i} = \beta\sum_{K\in\mathcal{T}_h^f} h_K^2(\boldsymbol{f}_f, \nabla\phi_{i,f})_K,\ F_{p,i} = \left(f_p, \phi_{i,p}\right)_{\Omega_p}.$$

Here $\boldsymbol{\Phi}_{i,f}$, $\phi_{i,f}$ and $\phi_{i,p}$ are the basis functions of $\boldsymbol{V}_{f,h}^0$, $W_{f,h}$ and $W_{p,h}$, respectively.

3 | A CONVERGENCE THEORY

In the space $\boldsymbol{V}_{f,h}^0 \times W_{f,h} \times W_{p,h}$, following[39], we define the parameter dependent norm

$$\begin{aligned}
|||[\boldsymbol{u}_{f,h}, p_{f,h}, p_{p,h}]|||_h^2 =& \frac{\rho}{\Delta t}\|\boldsymbol{u}_{f,h}\|_{0,\Omega_f}^2 + \mu\|\nabla\boldsymbol{u}_{f,h}\|_{0,\Omega_f}^2 + \frac{1}{\mu + \frac{\rho}{\Delta t}}\|p_{f,h}\|_{0,\Omega_f}^2 \\
&+ \beta\sum_{K\in\mathcal{T}_h^f} h_K^2\|\nabla p_{f,h}\|_{0,K}^2 + \frac{S_0}{\Delta t}\|p_{p,h}\|_{0,\Omega_p}^2 + \lambda_{\min}(\mathbb{K})\|\nabla p_{p,h}\|_{0,\Omega_p}^2.
\end{aligned} \tag{10}$$

Denote by $\mathcal{A}(\cdot,\cdot)$ the bilinear form of the discretized system (8), i.e.,

$$\begin{aligned}
&\mathcal{A}([\boldsymbol{u}_{f,h}, p_{f,h}, p_{p,h}], [\boldsymbol{v}_{f,h}, q_{f,h}, q_{p,h}]) \\
&= \left(\frac{\rho}{\Delta t}\boldsymbol{u}_{f,h}, \boldsymbol{v}_{f,h}\right)_{\Omega_f} + \left(\frac{S_0}{\Delta t}p_{p,h}, q_{p,h}\right)_{\Omega_p} + a([\boldsymbol{u}_{f,h}, p_{p,h}], [\boldsymbol{v}_{f,h}, q_{p,h}]) + b(\boldsymbol{v}_{f,h}, p_{f,h}) \\
&\quad - b(\boldsymbol{u}_{f,h}, q_{f,h}) + \beta \sum_{K\in\mathcal{T}_h^f} h_K^2 \frac{\rho}{\Delta t}\left(\boldsymbol{u}_{f,h}, \nabla q_{f,h}\right)_K + \beta \sum_{K\in\mathcal{T}_h^f} h_K^2 (\nabla p_{f,h}, \nabla q_{f,h})_K.
\end{aligned}$$

We first obtain the stability of the bilinear form $\mathcal{A}(\cdot,\cdot)$ with respect to the norm (10).

Lemma 1. Suppose that $\Delta t > \beta\rho h^2/2$, then for any $[\boldsymbol{u}_{f,h}, p_{f,h}, p_{p,h}]$ in $\boldsymbol{V}_{f,h}^0 \times W_{f,h} \times W_{p,h}$, there exists $[\boldsymbol{v}_{f,h}, q_{f,h}, q_{p,h}]$ in $\boldsymbol{V}_{f,h}^0 \times W_{f,h} \times W_{p,h}$, such that

$$\mathcal{A}([\boldsymbol{u}_{f,h}, p_{f,h}, p_{p,h}], [\boldsymbol{v}_{f,h}, q_{f,h}, q_{p,h}]) \gtrsim |||[\boldsymbol{u}_{f,h}, p_{f,h}, p_{p,h}]|||_h \, |||[\boldsymbol{v}_{f,h}, q_{f,h}, q_{p,h}]|||_h, \tag{11}$$

where $h = \max_{K\in\mathcal{T}_h^f} h_K$ is the mesh size of $\mathcal{T}_h^f$.

Proof. Assuming $[\boldsymbol{v}_{f,h}^1, q_{f,h}^1, q_{p,h}^1] = [\boldsymbol{u}_{f,h}, p_{f,h}, p_{p,h}]$, using the Schwarz and Korn's inequalities, we have

$$\begin{aligned}
&\mathcal{A}([\boldsymbol{u}_{f,h}, p_{f,h}, p_{p,h}], [\boldsymbol{v}_{f,h}^1, q_{f,h}^1, q_{p,h}^1]) = \mathcal{A}([\boldsymbol{u}_{f,h}, p_{f,h}, p_{p,h}], [\boldsymbol{u}_{f,h}, p_{f,h}, p_{p,h}]) \\
&\geqslant \frac{\rho}{\Delta t}\|\boldsymbol{u}_{f,h}\|_{0,\Omega_f}^2 + \frac{S_0}{\Delta t}\|p_{p,h}\|_{0,\Omega_p}^2 + 2\mu\|\mathbb{D}(\boldsymbol{u}_{f,h})\|_{0,\Omega_f}^2 + \alpha\|\boldsymbol{\tau}\cdot\boldsymbol{u}_{f,h}\|_{0,\Gamma}^2 + \lambda_{\min}(\mathbb{K})\|\nabla p_{p,h}\|_{0,\Omega_p}^2 \\
&\quad + \beta\frac{\rho}{\Delta t}\sum_{K\in\mathcal{T}_h^f} h_K^2\left(\boldsymbol{u}_{f,h}, \nabla p_{f,h}\right)_K + \beta\sum_{K\in\mathcal{T}_h^f} h_K^2\|\nabla p_{f,h}\|_{0,K}^2 \\
&\gtrsim \frac{\rho}{\Delta t}\|\boldsymbol{u}_{f,h}\|_{0,\Omega_f}^2 + \frac{S_0}{\Delta t}\|p_{p,h}\|_{0,\Omega_p}^2 + \mu\|\nabla\boldsymbol{u}_{f,h}\|_{0,\Omega_f}^2 + \lambda_{\min}(\mathbb{K})\|\nabla p_{p,h}\|_{0,\Omega_p}^2 \\
&\quad - \frac{\rho}{2\Delta t}\|\boldsymbol{u}_{f,h}\|_{0,\Omega_f}^2 - \beta^2\frac{\rho}{2\Delta t}\sum_{K\in\mathcal{T}_h^f} h_K^4\|\nabla p_{f,h}\|_{0,K}^2 + \beta\sum_{K\in\mathcal{T}_h^f} h_K^2\|\nabla p_{f,h}\|_{0,K}^2 \\
&\gtrsim \frac{\rho}{2\Delta t}\|\boldsymbol{u}_{f,h}\|_{0,\Omega_f}^2 + \frac{S_0}{\Delta t}\|p_{p,h}\|_{0,\Omega_p}^2 + \mu\|\nabla\boldsymbol{u}_{f,h}\|_{0,\Omega_f}^2 + \lambda_{\min}(\mathbb{K})\|\nabla p_{p,h}\|_{0,\Omega_p}^2 \\
&\quad + \beta\sum_{K\in\mathcal{T}_h^f}\left(1 - \frac{\beta\rho}{2\Delta t}h_K^2\right)h_K^2\|\nabla p_{f,h}\|_{0,K}^2 \\
&\gtrsim \frac{\rho}{2\Delta t}\|\boldsymbol{u}_{f,h}\|_{0,\Omega_f}^2 + \mu\|\nabla\boldsymbol{u}_{f,h}\|_{0,\Omega_f}^2 + \frac{S_0}{\Delta t}\|p_{p,h}\|_{0,\Omega_p}^2 + \lambda_{\min}(\mathbb{K})\|\nabla p_{p,h}\|_{0,\Omega_p}^2 \\
&\quad + \beta\left(1 - \frac{\beta\rho}{2\Delta t}h^2\right)\sum_{K\in\mathcal{T}_h^f} h_K^2\|\nabla p_{f,h}\|_{0,K}^2.
\end{aligned} \tag{12}$$

The coefficient of the term $\|\nabla p_{f,h}\|_{0,K}$ is positive when $\Delta t > \beta\rho h^2/2$. Observe that only the term $\|p_{f,h}\|_{0,\Omega_f}^2$ of the norm $|||\cdot|||_h$ is missing in the right-hand side of (12). To deal with it, note that the inf-sup condition is satisfied for the bilinear form $b(\cdot,\cdot)$ on $\boldsymbol{H}_0^1(\Omega_f) \times L^2(\Omega_f)$[40], it implies that for all $p_{f,h} \in W_{f,h}$, there exists $\boldsymbol{v}_{p_f} \in \boldsymbol{H}_0^1(\Omega_f)$, such that

$$-(p_{f,h}, \nabla\cdot\boldsymbol{v}_{p_f}) \gtrsim \|p_{f,h}\|_{0,\Omega_f}\|\nabla\boldsymbol{v}_{p_f}\|_{0,\Omega_f} \gtrsim \frac{1}{\sqrt{\mu + \frac{\rho}{\Delta t}}}\|p_{f,h}\|_{0,\Omega_f}\left(\sqrt{\mu + \frac{\rho}{\Delta t}}\|\nabla\boldsymbol{v}_{p_f}\|_{0,\Omega_f} + \sqrt{\frac{\rho}{\Delta t}}\|\boldsymbol{v}_{p_f}\|_{0,\Omega_f}\right),$$

where the second inequality holds by applying the Poincaré inequality. We now choose $\boldsymbol{v}_{p_f}$ such that

$$\sqrt{\mu + \frac{\rho}{\Delta t}}\|\nabla\boldsymbol{v}_{p_f}\|_{0,\Omega_f} + \sqrt{\frac{\rho}{\Delta t}}\|\boldsymbol{v}_{p_f}\|_{0,\Omega_f} = \frac{1}{\sqrt{\mu + \frac{\rho}{\Delta t}}}\|p_{f,h}\|_{0,\Omega_f}.$$

Let $\tilde{\boldsymbol{v}}_{p_f}$ be the Scott-Zhang or Clément interpolant (see[42]) of $\boldsymbol{v}_{p_f}$ to the finite element space $\left[S_h^f\right]^3 \cap \boldsymbol{H}_0^1(\Omega_f)$, a subspace of $\boldsymbol{V}_{f,h}^0$. Using the continuity of the interpolation, we have

$$\sqrt{\mu + \frac{\rho}{\Delta t}}\|\nabla(\tilde{\boldsymbol{v}}_{p_f})\|_{0,\Omega_f} + \sqrt{\frac{\rho}{\Delta t}}\|\tilde{\boldsymbol{v}}_{p_f}\|_{0,\Omega_f} \lesssim \frac{1}{\sqrt{\mu + \frac{\rho}{\Delta t}}}\|p_{f,h}\|_{0,\Omega_f}.$$

Now we set $[\boldsymbol{v}_{f,h}^2, q_{f,h}^2, q_{p,h}^2] = [\tilde{\boldsymbol{v}}_{p_f}, 0, 0]$, then using the Schwarz, Young's inequalities, the optimal estimate of the interpolation and the fact $\tilde{\boldsymbol{v}}_{p_f}|_{\partial\Omega_f} = 0$, we obtain

$$\begin{aligned}
&\mathcal{A}([\boldsymbol{u}_{f,h}, p_{f,h}, p_{p,h}], [\boldsymbol{v}_{f,h}^2, q_{f,h}^2, q_{p,h}^2]) = \mathcal{A}([\boldsymbol{u}_{f,h}, p_{f,h}, p_{p,h}], [\tilde{\boldsymbol{v}}_{p_f}, 0, 0]) \\
&= \left(\frac{\rho}{\Delta t}\boldsymbol{u}_{f,h}, \tilde{\boldsymbol{v}}_{p_f}\right)_{\Omega_f} + \left(2\mu\mathbb{D}(\boldsymbol{u}_{f,h}), \mathbb{D}(\tilde{\boldsymbol{v}}_{p_f})\right)_{\Omega_f} - \left(p_{f,h}, \nabla\cdot\boldsymbol{v}_{p_f}\right)_{\Omega_f} - \left(p_{f,h}, \nabla\cdot(\tilde{\boldsymbol{v}}_{p_f} - \boldsymbol{v}_{p_f})\right)_{\Omega_f} \\
&\gtrsim -\frac{\rho}{\Delta t}\|\boldsymbol{u}_{f,h}\|_{0,\Omega_f}\|\tilde{\boldsymbol{v}}_{p_f}\|_{0,\Omega_f} - \mu\|\mathbb{D}(\boldsymbol{u}_{f,h})\|_{0,\Omega_f}\|\mathbb{D}(\tilde{\boldsymbol{v}}_{p_f})\|_{0,\Omega_f} + \frac{1}{\mu + \frac{\rho}{\Delta t}}\|p_{f,h}\|_{0,\Omega_f}^2 \\
&\quad + \sum_{K\in\mathcal{T}_h^f}\left(\nabla p_{f,h}, \tilde{\boldsymbol{v}}_{p_f} - \boldsymbol{v}_{p_f}\right)_K \\
&\gtrsim -\frac{\eta_1\rho}{\Delta t}\|\boldsymbol{u}_{f,h}\|_{0,\Omega_f}^2 - \frac{\rho}{\eta_1\Delta t}\|\tilde{\boldsymbol{v}}_{p_f}\|_{0,\Omega_f}^2 - \eta_2\left(\frac{\mu}{\mu + \frac{\rho}{\Delta t}}\right)\mu\|\nabla(\boldsymbol{u}_{f,h})\|_{0,\Omega_f}^2 \\
&\quad - \frac{\mu + \frac{\rho}{\Delta t}}{\eta_2}\|\nabla(\tilde{\boldsymbol{v}}_{p_f})\|_{0,\Omega_f}^2 + \frac{1}{\mu + \frac{\rho}{\Delta t}}\|p_{f,h}\|_{0,\Omega_f}^2 - \sum_{K\in\mathcal{T}_h^f} h_K\|\nabla p_{f,h}\|_{0,K}\|\nabla\boldsymbol{v}_{p_f}\|_{0,K} \\
&\gtrsim \frac{1}{\mu + \frac{\rho}{\Delta t}}\left(1 - \frac{1}{\eta_1} - \frac{1}{\eta_2} - \frac{1}{\eta_3}\right)\|p_{f,h}\|_{0,\Omega_f}^2 - \eta_1\frac{\rho}{\Delta t}\|\boldsymbol{u}_{f,h}\|_{0,\Omega_f}^2 \\
&\quad - \eta_2\left(\frac{\mu}{\mu + \frac{\rho}{\Delta t}}\right)\mu\|\nabla(\boldsymbol{u}_{f,h})\|_{0,\Omega_f}^2 - \frac{\eta_3}{\beta\left(\mu + \frac{\rho}{\Delta t}\right)}\beta\sum_{K\in\mathcal{T}_h^f} h_K^2\|\nabla p_{f,h}\|_{0,K}^2,
\end{aligned} \tag{13}$$

for any constant $\eta_i > 0$, $i = 1, 2, 3$. Setting $[\boldsymbol{v}_{f,h}, q_{f,h}, q_{p,h}] = \sum_{i=1}^{2}\alpha_i[\boldsymbol{v}_{f,h}^i, q_{f,h}^i, q_{p,h}^i]$, and note that

$$|||[\boldsymbol{v}_{f,h}, q_{f,h}, q_{p,h}]|||_h \lesssim |||[\boldsymbol{u}_{f,h}, p_{f,h}, p_{p,h}]|||_h,$$

for any combination of coefficients $\alpha_i \in \mathbb{R}$. Therefore, the result follows by taking properly large $\eta_j, j = 1, 2, 3$ and suitable coefficients α_1 and α_2, such as $\eta_j = 4$ for $j = 1, 2, 3$, and $\alpha_1 = 1/C_1, \alpha_2 = 1/(16C_2)$, where C_1 and C_2 are the constants implied in (12) and (13), respectively. □

Next, we focus on the error estimate. To simplify the analysis, we just estimate the error from the spatial discretization. For this reason, we consider the following generalized Stokes-Darcy problem

$$\begin{aligned}
\frac{\rho}{\Delta t}\boldsymbol{u}_f - \nabla\cdot\mathbb{T}(\boldsymbol{u}_f, p_f) &= \boldsymbol{f}_f, \quad \text{in } \Omega_f \\
\nabla\cdot\boldsymbol{u}_f &= 0, \quad \text{in } \Omega_f \\
\frac{S_0}{\Delta t}p_p - \nabla\cdot(\mathbb{K}\nabla p_p) &= f_p, \quad \text{in } \Omega_p
\end{aligned} \tag{14}$$

with the same interface conditions (3)–(5) and boundary conditions (6). Similarly, we obtain the weak formulation of the problem (14) with (3)–(6): find $\boldsymbol{u}_f \in V_f$, $p_f \in W_f$, $p_p \in W_p$, such that

$$\begin{aligned}
&\frac{\rho}{\Delta t}\left(\boldsymbol{u}_f, \boldsymbol{v}_f\right)_{\Omega_f} + \frac{S_0}{\Delta t}\left(p_p, q_p\right)_{\Omega_p} + a([\boldsymbol{u}_f, p_p], [\boldsymbol{v}_f, q_p]) + b(\boldsymbol{v}_f, p_f) - b(\boldsymbol{u}_f, q_f) \\
&= (\boldsymbol{f}_f, \boldsymbol{v}_f)_{\Omega_f} + (f_p, q_p)_{\Omega_p} - (p_O, \boldsymbol{v}_f\cdot\boldsymbol{n}_f)_{\Gamma_O},
\end{aligned} \tag{15}$$

for all $\boldsymbol{v}_f \in V_f^0$, $q_f \in W_f$ and $q_p \in W_p$. The discretized form with stabilization is to find $\boldsymbol{u}_{f,h} \in \boldsymbol{V}_{f,h}$, $p_{f,h} \in W_{f,h}$, $p_{p,h} \in W_{p,h}$, such that

$$\begin{aligned}\mathcal{A}([\boldsymbol{u}_{f,h}, p_{f,h}, p_{p,h}], [\boldsymbol{v}_{f,h}, q_{f,h}, q_{p,h}]) =& (\boldsymbol{f}_f, \boldsymbol{v}_{f,h})_{\Omega_f} + (f_p, q_{p,h})_{\Omega_p} - (p_O, \boldsymbol{v}_{f,h} \cdot \boldsymbol{n}_f)_{\Gamma_O} \\ &+ \beta \sum_{K \in \mathcal{T}_h^f} h_K^2 (\boldsymbol{f}_f, \nabla q_{f,h})_K,\end{aligned} \tag{16}$$

for all $\boldsymbol{v}_{f,h} \in \boldsymbol{V}_{f,h}^0$, $q_{f,h} \in W_{f,h}$, $q_{p,h} \in W_{p,h}$. The stabilized form (16) has the same bilinear form as (8). Compared with (8), the only difference of (16) is that the terms related to the temporal discretization in the right-hand side are ignored. Suppose $\boldsymbol{u}_f \in \boldsymbol{H}^2(\Omega_f)$, $p_f \in H^1(\Omega_f)$ and $p_p \in H^2(\Omega_p)$, then $\boldsymbol{u}_f$, p_f and p_p are continuous and we can define $\Pi_h \boldsymbol{u}_f$, $\Pi_h p_f$ and $\Pi_h p_p$ as suitable interpolants of $\boldsymbol{u}_f$, p_f and p_p to the corresponding finite element space, respectively, satisfying optimal interpolation estimates. Define the error function

$$E(h)^2 = \frac{\rho}{\Delta t}\varepsilon_0^2(\boldsymbol{u}_f) + \mu\varepsilon_1^2(\boldsymbol{u}_f) + \frac{1}{\mu}\varepsilon_0^2(p_f) + \beta \sum_{K \in \mathcal{T}_h^f} h_K^2 \varepsilon_{1,K}^2(p_f) + \frac{S_0}{\Delta t}\varepsilon_0^2(p_p) + \lambda_{\max}(\mathbb{K})\varepsilon_1^2(p_p), \tag{17}$$

where $\varepsilon_i(\boldsymbol{u}_f), \varepsilon_i(p_f)$ and $\varepsilon_i(p_p)$ are the corresponding interpolation errors in the norm of $\boldsymbol{H}^i(\Omega_f), H^i(\Omega_f)$ and $H^i(\Omega_p)$, respectively, and $\varepsilon_{1,K}(p_f)$ represents the interpolation error in element K. Then, we have

$$|||[\Pi_h \boldsymbol{u}_f - \boldsymbol{u}_f, \Pi_h p_f - p_f, \Pi_h p_p - p_p]|||_h \lesssim E(h). \tag{18}$$

Theorem 1. Let $(\boldsymbol{u}_f, p_f, p_p)$ and $(\boldsymbol{u}_{f,h}, p_{f,h}, p_{p,h})$ be the solution of (15) and (16), respectively. Suppose $\boldsymbol{u}_f \in \boldsymbol{H}^2(\Omega_f)$, $p_f \in H^2(\Omega_f)$ and $p_p \in H^2(\Omega_p)$, and the assumption of Lemma 1 holds, then

$$|||[\boldsymbol{u}_f - \boldsymbol{u}_{f,h}, p_f - p_{f,h}, p_p - p_{p,h}]|||_h \lesssim E(h). \tag{19}$$

Proof. Denote by $\boldsymbol{e}_{\boldsymbol{u}_f} = \boldsymbol{u}_f - \boldsymbol{u}_{f,h}$, $e_{p_f} = p_f - p_{f,h}$ and $e_{p_p} = p_p - p_{p,h}$. Subtracting (16) from (15), we obtain the error equations

$$\begin{aligned}\mathcal{A}([\boldsymbol{e}_{\boldsymbol{u}_f}, e_{p_f}, e_{p_p}], [\upsilon_{f,h}, q_{f,h}, q_{p,h}]) =& \beta \sum_{K \in \mathcal{T}_h^f} h_K^2 \left(\frac{\rho}{\Delta t}\boldsymbol{u}_f + \nabla p_f - \boldsymbol{f}_f, \nabla q_{f,h} \right)_K \\ =& \beta \sum_{K \in \mathcal{T}_h^f} h_K^2 (\nabla \cdot (2\mu\mathbb{D}(\boldsymbol{u}_f)), \nabla q_{f,h})_K.\end{aligned} \tag{20}$$

Using $\boldsymbol{e}_{\boldsymbol{u}_f} = (\Pi_h \boldsymbol{u}_f - \boldsymbol{u}_{f,h}) - (\Pi_h \boldsymbol{u}_f - \boldsymbol{u}_f)$, $e_{p_f} = (\Pi_h p_f - p_{f,h}) - (\Pi_h p_f - p_f)$, and $e_{p_p} = (\Pi_h p_p - p_{p,h}) - (\Pi_h p_p - p_p)$, the error equations (20) can be rewritten as

$$\begin{aligned}&\mathcal{A}([\Pi_h \boldsymbol{u}_f - \boldsymbol{u}_{f,h}, \Pi_h p_f - p_{f,h}, \Pi_h p_p - p_{p,h}], [\upsilon_{f,h}, q_{f,h}, q_{p,h}]) \\ &= \mathcal{A}([\Pi_h \boldsymbol{u}_f - \boldsymbol{u}_f, \Pi_h p_f - p_f, \Pi_h p_p - p_p], [\upsilon_{f,h}, q_{f,h}, q_{p,h}]) + \beta \sum_{K \in \mathcal{T}_h^f} h_K^2 (\nabla \cdot (2\mu\mathbb{D}(\boldsymbol{u}_f)), \nabla q_{f,h})_K.\end{aligned} \tag{21}$$

From Lemma 1, there exists $[\boldsymbol{v}_{f,h}, q_{f,h}, q_{p,h}]$ such that

$$\begin{aligned}&|||\ [\Pi_h \boldsymbol{u}_f - \boldsymbol{u}_{f,h}, \Pi_h p_f - p_{f,h}, \Pi_h p_p - p_{p,h}]\ |||_h\ |||[\boldsymbol{v}_{f,h}, q_{f,h}, q_{p,h}]|||_h \\ &\lesssim \mathcal{A}([\Pi_h \boldsymbol{u}_f - \boldsymbol{u}_{f,h}, \Pi_h p_f - p_{f,h}, \Pi_h p_p - p_{p,h}], [\boldsymbol{v}_{f,h}, q_{f,h}, q_{p,h}]) \\ &= \mathcal{A}([\Pi_h \boldsymbol{u}_f - \boldsymbol{u}_f, \Pi_h p_f - p_f, \Pi_h p_p - p_p], [\upsilon_{f,h}, q_{f,h}, q_{p,h}]) + \beta \sum_{K \in \mathcal{T}_h^f} h_K^2 (\nabla \cdot (2\mu\mathbb{D}(\boldsymbol{u}_f)), \nabla q_{f,h})_K.\end{aligned} \tag{22}$$

Using the finite element inverse inequality and the trace inequality

$$\|v\|_{0,\partial K}^2 \lesssim (h_K^{-1}\|v\|_{0,K} + h_K\|\nabla v\|_{0,K}^2), \forall v \in H^1(K), K \in \mathcal{T}_h,$$

from the definition of $\mathcal{A}(\cdot,\cdot)$, the first term in the right-hand side of (22) can be bounded as follows:

$$
\begin{aligned}
&\mathcal{A}([\Pi_h \boldsymbol{u}_f - \boldsymbol{u}_f, \Pi_h p_f - p_f, \Pi_h p_p - p_p], [\boldsymbol{v}_{f,h}, q_{f,h}, q_{p,h}]) \\
&= \frac{\rho}{\Delta t}(\Pi_h \boldsymbol{u}_f - \boldsymbol{u}_f, \boldsymbol{v}_{f,h})_{\Omega_f} + 2\mu(\mathbb{D}(\Pi_h \boldsymbol{u}_f - \boldsymbol{u}_f), \mathbb{D}(\boldsymbol{v}_{f,h}))_{\Omega_f} - (\Pi_h p_f - p_f, \nabla \cdot \boldsymbol{v}_{f,h})_{\Omega_f} \\
&\quad + (\nabla \cdot (\Pi_h \boldsymbol{u}_f - \boldsymbol{u}_f), q_{f,h})_{\Omega_f} + \frac{S_0}{\Delta t}(\Pi_h p_p - p_p, q_{p,h})_{\Omega_p} + (\mathbb{K}\nabla(\Pi_h p_p - p_p), \nabla q_{p,h})_{\Omega_p} \\
&\quad + \beta \frac{\rho}{\Delta t} \sum_{K \in \mathcal{T}_h^f} h_K^2 (\Pi_h \boldsymbol{u}_f - \boldsymbol{u}_f, \nabla q_{f,h})_K + \beta \sum_{K \in \mathcal{T}_h^f} h_K^2 (\nabla(\Pi_h p_f - p_f), \nabla q_{f,h})_K \\
&\quad + \sum_{i=1}^{2} \alpha(\boldsymbol{\tau}_i \cdot (\Pi_h \boldsymbol{u}_f - \boldsymbol{u}_f), \boldsymbol{\tau}_i \cdot \boldsymbol{v}_{f,h})_\Gamma + (\Pi_h p_p - p_p, \boldsymbol{v}_{f,h} \cdot \boldsymbol{n}_f)_\Gamma - ((\Pi_h \boldsymbol{u}_f - \boldsymbol{u}_f) \cdot \boldsymbol{n}_f, q_{p,h})_\Gamma \\
&\lesssim \frac{\rho}{\Delta t}\varepsilon_0(\boldsymbol{u}_f)\|\boldsymbol{v}_{f,h}\|_{0,\Omega_f} + \mu\varepsilon_1(\boldsymbol{u}_f)\|\nabla \boldsymbol{v}_{f,h}\|_{0,\Omega_f} + \varepsilon_0(p_f)\|\nabla \boldsymbol{v}_{f,h}\|_{0,\Omega_f} + \varepsilon_1(\boldsymbol{u}_f)\|q_{f,h}\|_{0,\Omega_f} \\
&\quad + \frac{S_0}{\Delta t}\varepsilon_0(p_p)\|q_{p,h}\|_{0,\Omega_p} + \lambda_{\max}(\mathbb{K})\varepsilon_1(p_p)\|\nabla q_{p,h}\|_{0,\Omega_p} + \frac{\beta\rho}{\Delta t}\varepsilon_0(\boldsymbol{u}_f) \sum_{K \in \mathcal{T}_h^f} h_K^2 \|\nabla q_{f,h}\|_{0,K} \\
&\quad + \beta\varepsilon_1(p_f) \sum_{K \in \mathcal{T}_h^f} h_K^2 \|\nabla q_{f,h}\|_{0,K} + \alpha(h^{-1}\varepsilon_0(\boldsymbol{u}_f) + \varepsilon_1(\boldsymbol{u}_f))\|\boldsymbol{v}_{f,h}\|_{0,\Omega_f} \\
&\quad + (h^{-1}\varepsilon_0(p_p) + \varepsilon_1(p_p))\|\boldsymbol{v}_{f,h}\|_{0,\Omega_f} + (h^{-1}\varepsilon_0(\boldsymbol{u}_f) + \varepsilon_1(\boldsymbol{u}_f))\|q_{p,h}\|_{0,\Omega_p} \\
&\lesssim E(h) \,|||\, [\boldsymbol{v}_{f,h}, q_{f,h}, q_{p,h}] \,|||_h \,.
\end{aligned} \tag{23}
$$

For the second term in the right-hand side of (22), using the Schwarz inequality, we have

$$
\begin{aligned}
&\beta \sum_{K \in \mathcal{T}_h^f} h_K^2 (\nabla \cdot (2\mu\mathbb{D}(\boldsymbol{u}_f)), \nabla q_{f,h})_K \\
&\lesssim \beta\mu \sum_{K \in \mathcal{T}_h^f} h_K^2 \|\boldsymbol{u}_f\|_{2,K} \|\nabla q_{f,h}\|_{0,K} \lesssim E(h) \,|||\, [\boldsymbol{v}_{f,h}, q_{f,h}, q_{p,h}] \,|||_h \,.
\end{aligned} \tag{24}
$$

We finally obtain the result by combining (17) with (22)–(24) and using the triangle inequality. □

Remark 1. From Theorem 1, assume that the mesh $\mathcal{T}_h$ is quasi-uniform, we have the error estimate

$$
\begin{aligned}
&\frac{\rho}{\Delta t}\|\boldsymbol{e}_{\boldsymbol{u}_f}\|_{0,\Omega_f}^2 + \mu\|\nabla \boldsymbol{e}_{\boldsymbol{u}_f}\|_{0,\Omega_f}^2 + \frac{1}{\mu + \frac{\rho}{\Delta t}}\|e_{p_f}\|_{0,\Omega_f}^2 + \beta \sum_{K \in \mathcal{T}_h^f} h_K^2 \|\nabla e_{p_f}\|_{0,K}^2 \\
&\quad + \frac{S_0}{\Delta t}\|e_{p_p}\|_{0,\Omega_p}^2 + \lambda_{\min}(\mathbb{K})\|\nabla e_{p_p}\|_{0,\Omega_p}^2 \\
&\lesssim \left(\frac{\rho h^2}{\Delta t} + \mu\right) h^2 \|\boldsymbol{u}_f\|_{2,\Omega_f}^2 + \left(\frac{1}{\mu} + \beta\right) h^2 \|p_f\|_{1,\Omega_f}^2 + \left(\frac{S_0 h^2}{\Delta t} + \lambda_{\max}(\mathbb{K})\right) h^2 \|p_p\|_{2,\Omega_p}^2.
\end{aligned} \tag{25}
$$

The error estimates of $\boldsymbol{u}_f$ and p_p are optimal in H^1- and L^2-norm provided $\Delta t = O(h^2)$.

4 | TWO-LEVEL ADDITIVE SCHWARZ PRECONDITIONER WITH A MIXED-DIMENSIONAL COARSE SPACE

To solve the large-scale linear systems (9), we use a Krylov subspace method with an additive Schwarz preconditioner. We divide the domains Ω_f and Ω_p into np_1 and np_2 nonoverlapping subdomains, respectively, see Fig. 2. Denote by $np = np_1 + np_2$ the total number of subdomains. Each nonoverlapping subdomain $\Omega_i^0, i = 1, \ldots, np$ is extended to include δ layers of elements from adjacent subdomains to form the overlapping subdomain Ω_i. Note that the fluid subdomains and the porous medium subdomains do not overlap each other. Considering the scalability and effectiveness, in this section, we focus on the construction of a robust two-level Schwarz preconditioner. For the local part, we define R_i (R_i^0) as the natural restriction matrix corresponding to the subdomain Ω_i (Ω_i^0). In the practical implementation, the product of R_i and a vector v is equivalent to extracting elements from v based on the indexes listed in Ω_i. For the global part, denote R_c and E_c as the coarse restriction and extension matrices, respectively, and we usually define R_c as the transpose of E_c. The columns of E_c span the coarse space, which determines the

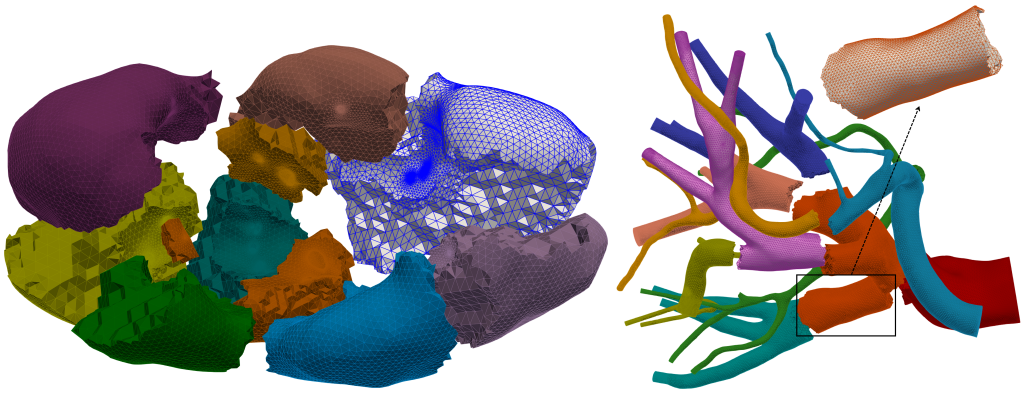

Figure 2 A sample mesh and a partition of the kidney tissue domain into subdomains (left) and the fluid domain into subdomains (right).

performance of the coarse preconditioner. The two-level Schwarz preconditioner M_{2s}^{-1} then can be represented in the form

$$M_{2s}^{-1} = \sum_{i=1}^{np} (R_i^0)^T A_i^{-1} R_i + E_c A_c^{-1} R_c := M_{1s}^{-1} + M_c^{-1}, \tag{26}$$

where $A_i = R_i A R_i^T$ is the local matrix restricted in the ith subdomain, M_{1s}^{-1} is the one-level preconditioner[43] and M_c^{-1} is the coarse preconditioner. The coarse matrix A_c can be obtained by the discretization in the coarse space or computed directly by $A_c = R_c A E_c$ adopted here. Following the idea of the mixed-dimensional coarse preconditioner in blood flow problems[44], we introduce a 1D-3D coarse preconditioner consisting of a 1D central-line coarse preconditioner in the vascular region and a 3D coarse preconditioner in the kidney tissue region.

4.1 | The construction of extension matrix E_c

Let E_f denote an extension matrix in the vascular region and E_p an extension matrix in the kidney tissue region. Then the extension matrix E_c takes the form

$$E_c = \begin{pmatrix} E_f & 0 \\ 0 & E_p \end{pmatrix}.$$

To construct E_f and E_p, we introduce a unified framework based on a set of coarse mesh points and the interpolation technique. Let $\left\{x_f^i\right\}_{i=1}^{N_f}$ be the set of fine mesh points and $\left\{x_c^i\right\}_{i=1}^{N_c}$ the set of coarse mesh points. For any continuous function $g(x)$, the interpolation is given by for the coarse basis functions $\left\{\varphi_i\right\}_{i=1}^{N_c}$,

$$\Pi_g(x) = \sum_{i=1}^{N_c} \alpha_i \varphi_i(x),$$

satisfying the equivalence in coarse interpolation points

$$\Pi_g(x_c^i) = g(x_c^i), \quad i = 1, \dots, N_c,$$

i.e.,

$$\Phi_{cc} \boldsymbol{\alpha} = G_c,$$

where $\Phi_{cc} = \left(\varphi_i(x_c^j)\right)$ is a $N_c \times N_c$ interpolation matrix , $\boldsymbol{\alpha} = [\alpha_1, \dots, \alpha_{N_c}]^T$ and $G_c = \left[g(x_c^1), \dots, g(x_c^{N_c})\right]^T$. Then the approximation of g on the fine mesh can be obtained by

$$G_f = \left[\Pi_g(x_f^1), \dots, \Pi_g(x_f^{N_f})\right]^T = \left(\Phi_{cf}\right)^T \Phi_{cc}^{-1} G_c = \left[\Phi_{cc}^{-1} \Phi_{cf}\right]^T G_c := \left(I_{cf}\right)^T G_c, \tag{27}$$

where $\Phi_{cf} = \left(\varphi_i(x_f^j)\right)$ is an $N_c \times N_f$ interpolation matrix and I_{cf}^T is called the extension matrix from the coarse mesh to the fine mesh. Note that for Lagrangian coarse basis functions, the interpolation matrix Φ_{cc} is the identity matrix and therefore

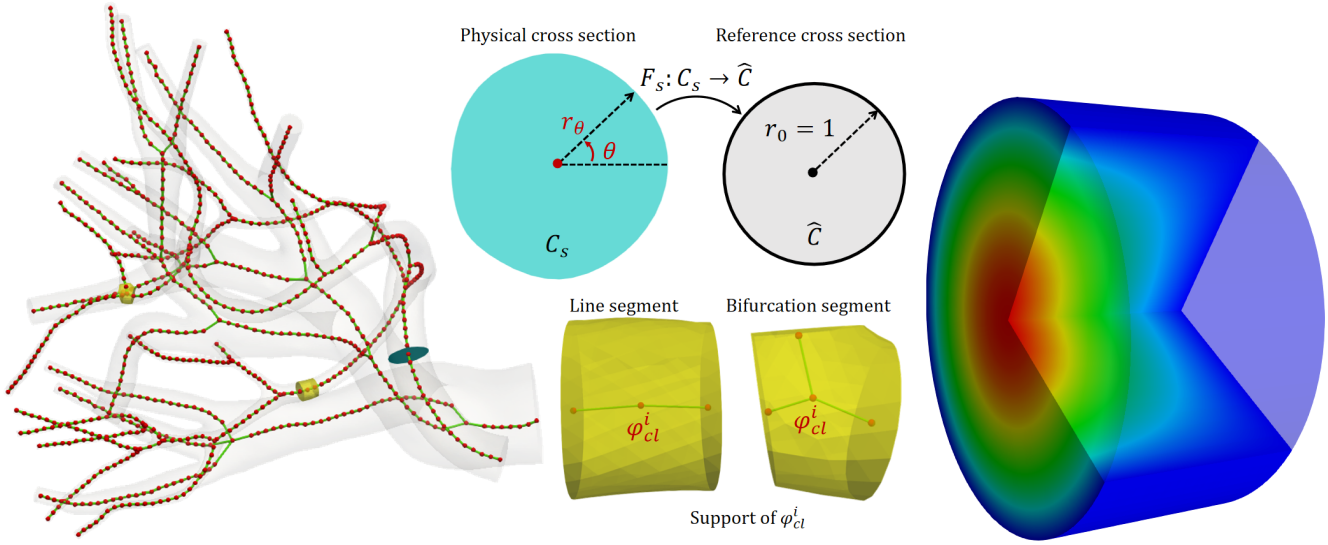

Figure 3 The centerline and mesh of renal vessels, cross sections, the support and the distribution of coarse basis functions

the extension matrix I^T_{cf} is reduced to Φ^T_{cf} whose entries are the value of coarse basis functions at fine mesh points. We next construct the extension matrices E_f and E_p by this framework with different coarse basis functions, respectively.

4.1.1 | The construction of E_f

Following[45], we construct E_f in Ω_f by a coarse mesh defined on the centerline Ω^{cl}_f, which is a curve with many branches in the three-dimensional space parameterized by the arc length s, see the left subfigure of Fig. 3. The centerline is divided into many sub-centerlines $\left\{\Omega^{cl}_{f,i}\right\}_{i=1}^{M}$ by the junctions and then we partition them to generate a coarse mesh with mesh points $\left\{x^i_{cl}\right\}_{i=1}^{N_{cl}}$ including the endpoints and bifurcation points. Denote by C^i_s the cross section at x^i_{cl}. For each mesh point x^i_{cl}, we define its influence region D_i as the part of Ω_f which is enclosed by the intersecting wall Γ_f and cross sections C^j_s ($j \in \mathcal{I}_i$) where $\mathcal{I}_i$ is the collection of adjacent central-line mesh points of x^i_{cl}, see the yellow regions of the left subfigure of Fig. 3. Now for the velocity, we define the coarse basis function associated with x^i_{cl} as $\boldsymbol{\varphi}^i_{cl}$ with the local support D_i. Specifically, it takes the form

$$\boldsymbol{\varphi}^i_{cl}(s, r, \theta) = \zeta\left(\frac{r(s)}{r_\theta(s)}\right)\phi^i_{cl}(s)\boldsymbol{\tau}^i_{cl}, \tag{28}$$

where the pair (r, θ) is the polar coordinates in C^i_s, $r_\theta(s)$ is the radial radius, $\boldsymbol{\tau}^i_{cl}$ is the unit tangential vectors of the centerline at x^i_{cl}, and ζ is a radial profile function

$$\zeta(y) = (1 - y^\gamma),\ y \in [0, 1], \tag{29}$$

with the profile parameter γ, and ϕ^i_{cl} is a linear Lagrangian basis function defined on the centerline, satisfying

$$\phi^i_{cl}(s(x^j_{cl})) = \delta_{ij}, \forall i, j = 1, \ldots, N_{cl}, \tag{30}$$

δ_{ij} being the Kronecker delta. In (28), $r(s)/r_\theta(s)$ is used to transform irregular physical cross sections C_s into the reference cross section $\hat{C}$. Considering the basis function $\boldsymbol{\varphi}^i_{cl}$ resembles a cone, we refer to it as a conical basis function in this context, shown in the right subfigure of Fig. 3. For the pressure we use ϕ^i_{cl} directly as the coarse basis function, which is simply an identity profile function. These settings of coarse basis functions are motivated by the observations and the assumption of the reduced blood flow model[46,45]. By the definition of these coarse basis functions, using the form (27), we obtain

$$E_f = \begin{pmatrix} \boldsymbol{W}_{u,cl} & 0 \\ 0 & W_{p,cl} \end{pmatrix}^T, \boldsymbol{W}_{u,cl} = (\boldsymbol{\varphi}^i_{cl}(x^j_f)),\ W_{p,cl} = (\phi^i_{cl}(x^j_f)), \tag{31}$$

where $\left\{x^i_f\right\}_{i=1}^{N_f}$ is the set of fine mesh points of $\mathcal{T}^f_h$. As the Lagrangian property (30), the interpolation matrix Φ_{cc} is diagonal and the computation of (31) does not require the solution of the interpolation system.

4.1.2 | The construction of E_p

For the porous medium region, we construct E_p using a set of coarse mesh points and the radial basis interpolation[44]. Without confusion, we use the same notation $\left\{x_c^i\right\}_{i=1}^{N_c}$ to denote the collocation of coarse mesh points of Ω_p. Note that the geometry of the kidney tissue is characterized by a multi-scale structure with a large outer boundary and many small inner boundaries outlined by the blood vessels and the kidney tissue. Therefore, the generation of a coarse mesh that accurately represents the small-scale inner boundaries is extremely challenging. In fact such an accurate coarse mesh may not be necessary as part of a coarse preconditioner[7]. For this reason, we introduce a non-nested coarse mesh generated independent of the fine mesh that provides a good match of the geometry of the outer boundary but only a very rough match for the geometry of the inner boundaries, as shown in Fig. 4. In this case, the coarse and fine meshes are not isogeometric, making the use of the linear Lagrangian interpolation unsuitable, especially near the inner boundaries. To address the issue, we define the coarse basis functions $\left\{\varphi_c^i\right\}_{i=1}^{N_c}$ using the Wendland radial basis function[47]

$$\varphi_c^i(x;\xi) = \begin{cases} \left(1-\frac{|x-x_c^i|}{\xi}\right)^4 \left(1+\frac{4|x-x_c^i|}{\xi}\right), & |x-x_c^i| \le \xi; \\ 0, & \text{otherwise}, \end{cases} \tag{32}$$

where ξ is the shape parameter. Since the function is not Lagrangian, it requires the solution of the interpolation system. To reduce the computational complexity, we adopt a local strategy, i.e., for each fine mesh point x_p^i, $i = 1, \dots, N_p$, finding s nearest coarse mesh points $\left\{x_c^{i_k}\right\}_{k=1}^{s}$ to obtain the interpolation approximation $\Pi_g(x_p^i)$ with $\xi = 2H_i$, where H_i is the diameter of the set $\left\{x_p^i, x_c^{i_1}, \dots, x_c^{i_s}\right\}$ defined as follows:

$$\begin{aligned} \Pi_g(x_p^i) &= [\varphi_c^{i_1}(x_p^i;\xi), \dots, \varphi_c^{i_s}(x_p^i;\xi)] \begin{pmatrix} \varphi_c^{i_1}(x_c^{i_1};\xi) & \dots & \varphi_c^{i_1}(x_c^{i_s};\xi) \\ \vdots & \ddots & \vdots \\ \varphi_c^{i_s}(x_c^{i_1};\xi) & \dots & \varphi_c^{i_s}(x_c^{i_s};\xi) \end{pmatrix}^{-1} \begin{pmatrix} g(x_c^{i_1}) \\ \vdots \\ g(x_c^{i_s}) \end{pmatrix} \\ &:= (\Phi_{cf}^i)^T \left(\Phi_{cc}^i\right)^{-1} G_c^i = \left[\left(\Phi_{cc}^i\right)^{-1} \Phi_{cf}^i\right]^T G_c^i := \left(I_{cf}^i\right)^T G_c^i. \end{aligned}$$

Denote by I_p^i a N_c-dimensional column vector satisfying

$$I_p^i(j) = \begin{cases} I_{cf}^i(k), & j = i_k, k = 1, \dots, s, \\ 0, & \text{otherwise}, \end{cases}$$

for $i = 1, \dots, N_p$. Then E_p is defined as

$$E_p = \left[I_p^1, \dots, I_p^{N_p}\right]^T. \tag{33}$$

Note that s is a suitable parameter to balance the interpolation accuracy and the computation cost. Given that most of the fine mesh points are inside the computational domain specified by the coarse mesh, the first four nearest coarse mesh points are exactly the vertices of a coarse element containing the fine mesh point, which is matched with the Lagrangian interpolation[7].

Remark 2. In the implementation of E_f, we scale I_{cf}^i by $\bar{I}_{cf}^i = I_{cf}^i / \sum I_{cf}^i$ to improve its accuracy as in[48]. Instead of the locally supported Wendland basis function used in this paper, other globally supported radial basis functions are also possible[44].

Remark 3. In this paper, we compute A_c directly by $E_c^T A E_c$ for simplicity. In fact it can also be obtained by the discretization of the following reduced coupled 1D Stokes and 3D Darcy equations:

1. On the centerline Ω_f^{cl}, we assume that the fluid satisfies the 1D Stokes equations[45,49]

$$\begin{cases} \rho\dfrac{A_s}{2}\dfrac{\partial u^{cl}}{\partial t} + \dfrac{K_r}{2}u^{cl} + A_s\dfrac{\partial p^{cl}}{\partial s} = f^{cl} \ \text{ in } \Omega_f^{cl}\times(0,T), \\ \dfrac{\partial}{\partial s}\left(A_s u^{cl}\right) = 0 \ \text{ in } \Omega_f^{cl}\times(0,T), \\ u^{cl}(s,0) = 0 \ \text{ in } \Omega_f^{cl}, \end{cases} \tag{34}$$

with the boundary conditions

$$u^{cl}(s_I,t) = -\frac{2}{|\Gamma_I|}\int_{\Gamma_I} \boldsymbol{u}_I\cdot\boldsymbol{n}\mathrm{d}\Gamma_I, \quad p^{cl}(s_O^i,t) = \frac{R_O^i A_s}{2}u^{cl}(s_O^i,t), \quad i = 1,\dots,m, \tag{35}$$

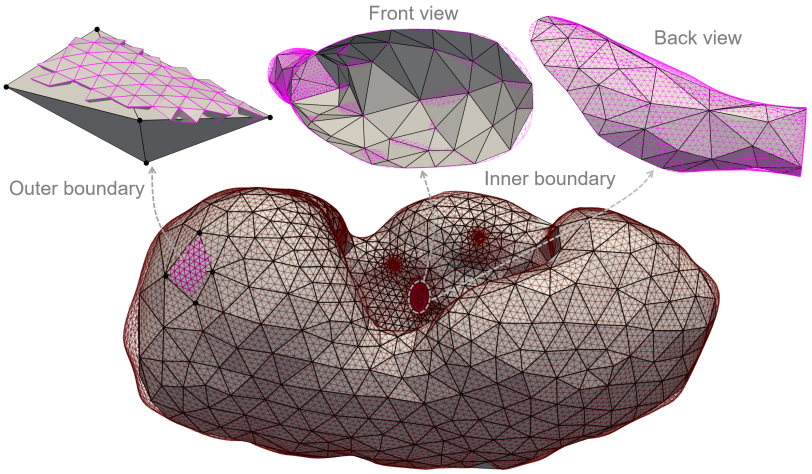

Figure 4 Non-nested coarse mesh (black) and fine mesh (light red) for the kidney tissue with local features at the outer and the inner boundaries.

and the bifurcation compatibility conditions

$$A_s(s^i_{J_1})u^{cl}(s^i_{J_1}) = A_s(s^i_{J_2})u^{cl}(s^i_{J_2}) + A_s(s^i_{J_3})u^{cl}(s^i_{J_3}), \tag{36}$$

$$p^{cl}(s^i_{J_1}) = p^{cl}(s^i_{J_2}) = p^{cl}(s^i_{J_3})\,(i = 1, \dots, m_J), \tag{37}$$

where $\alpha = 4/3$ is the Coriolis coefficient and $K_r = 8\pi\mu$.

2. In the porous medium region Ω_p, we assume that the kidney tissue satisfies the 3D Darcy equations

$$\begin{cases} S_0 \dfrac{\partial p_p}{\partial t} - \nabla \cdot (\mathbb{K}\nabla p_p) = f_p, & \text{in } \Omega_p \times (0, T], \\ p_p(x, 0) = p_{p,0}(x), & \text{in } \Omega_p. \end{cases} \tag{38}$$

3. On the interface $\Gamma = \overset{m_f}{\underset{i=1}{\cup}} \Gamma_i$, we assume the following compatibility conditions

$$u_i^{cl} = \text{sign}(\boldsymbol{u}\cdot\boldsymbol{n})\frac{2}{|\Gamma_i|}\int_{\Gamma_i} \boldsymbol{u}\cdot\boldsymbol{n}\mathrm{d}\Gamma_i, \quad p_i^{cl} = \frac{1}{|\Gamma_i|}\int_{\Gamma_i} p\mathrm{d}\Gamma_i\ (i = 1, \dots, m_f). \tag{39}$$

In (39), the first condition represents the conservation of mass across the interface and the second condition reflects the balance of normal forces on both sides of the interface, which can be derived from (3)–(4). As for the condition corresponding to the balance of tangential forces (5), it is neglected in the reduced model since the tangential components of the velocity are ignored.

Remark 4. For the comparison in the experiments, we also consider a 0D coarse preconditioner[46] where the coarse basis functions are the characteristic functions in the nonoverlapping subdomains for both Ω_f and Ω_p

$$\varphi_i(x) = \begin{cases} 1, & x \in \Omega_i^0, \\ 0, & \text{otherwise}, \end{cases} \tag{40}$$

and a 1D-0D coarse preconditioner where the coarse basis functions are the same as the proposed 1D-3D coarse preconditioner in the vascular region Ω_f but are replaced by the characteristic functions (40) in the kidney tissue region Ω_p.

5 | NUMERICAL EXPERIMENTS

In this section, some numerical experiments are presented to verify the theoretical results, and to study the performance of the proposed methods. We consider two geometries: (1) a simple geometry consisting of two tubes and a box whose sizes are close to the realistic main renal vessels and the kidney; (2) a patient-specific geometry including a renal arterial network, a renal

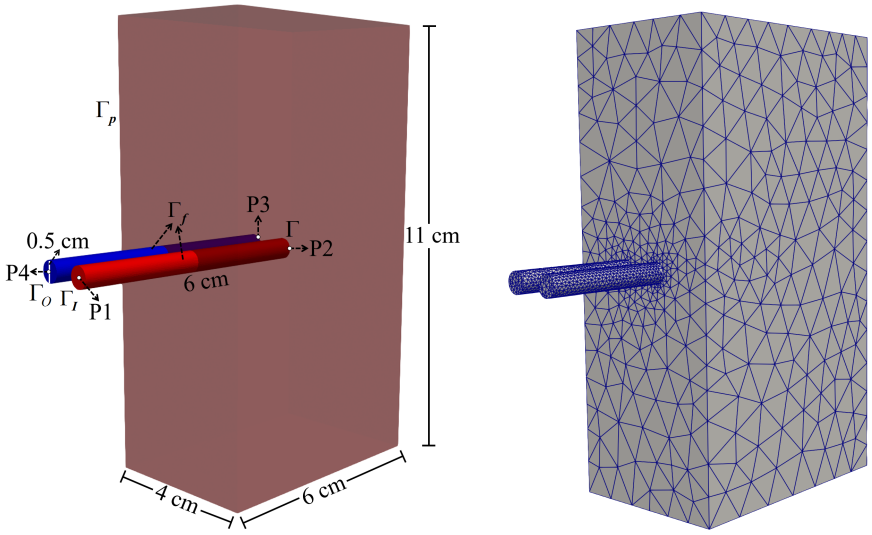

Figure 5 The left subfigure: the computed domain consisting of two tubes (representing the artery and vein marked in red and blue, respectively) and a box (representing the kidney) for Example 1 and 2, as well as four monitoring points: P1 on the inlet of artery, P2 on the outlet of vein, P3 and P4 on two interfaces; the right subfigure: a coarse unstructured mesh with 13810 mesh points.

venous network and a kidney. For simplicity, we focus on the isotropic and homogeneous permeability, i.e., $\mathbb{K} = k\mathbb{I}$, where k is a scalar permeability and $\mathbb{I}$ is the identity tensor. To solve the discretized systems, a right-preconditioned restarted GMRES(100) is used. The iteration is stopped if the relative tolerance 10^{-9} or the absolute tolerance 10^{-6} is reached. The maximal number of GMRES iterations is set to 600. To investigate the performance of the proposed preconditioner, we focus on four preconditioners including the one-level additive Schwarz preconditioner M_{1s}^{-1} and the two-level additive Schwarz preconditioners M_{2s}^{-1} with three different coarse preconditioners inlcuding the 0D coarse preconditioner, the 1D-0D coarse preconditioner and the 1D-3D coarse preconditioner. For these preconditioners, the LU and incomplete LU (ILU) factorizations are used as the coarse solver and subdomain solvers, respectively. In all experiments, np denotes the number of subdomains, and δ represents the number of the overlapping layers.

5.1 | Example 1: For the verification of the convergence rate

In this example, we consider a simple geometry as shown in the left figure of Fig. 5 and the parameters are set as follows: $\rho = 1$, $\mu = 1$, $\alpha = 1$, $S_0 = 1$ and $k = 1$. We set the source terms and boundary conditions to satisfy the exact solution

$$\boldsymbol{u}_f = \begin{pmatrix} (t+1)e^{\frac{-2x+y+z}{\mu}} \\ (t+1)e^{\frac{-2x+y+z}{\mu}} \\ (t+1)e^{\frac{-2x+y+z}{\mu}} \end{pmatrix}, \; p_f = \left(\frac{\mu}{2k} - 4\right)(t+1)e^{\frac{-2x+y+z}{\mu}}, \; p_p = \frac{\mu}{2k}(t+1)e^{\frac{-2x+y+z}{\mu}}.$$

To test the order of convergence, we generate an unstructured tetrahedral mesh with 13,810 mesh points (see the right of Fig. 5) and two gradually refined meshes with 98,248 and 741,373 mesh points. Table 1 shows the errors in L^2- and H^1-norm and numerical orders of convergence at the first time step ($\Delta t = 0.02$). We can see that these errors decrease gradually as the mesh is refined, and the velocity $\boldsymbol{u}_f$ and pressure p_p exhibit the optimal orders of convergence, i.e., the second and the first order in the L^2- and H^1-norm, respectively, which is consistent with our theory (25). Note that the pressure p_f in L^2-norm reaches the second-order convergence better than the theoretical estimate.

5.2 | Example 2: Some simulations in the simple geometry

In the second example, we carry out some simulations in the simple geometry and focus on the realistic settings for the boundary conditions and the parameters. We first set the source terms $\boldsymbol{f}_f = \boldsymbol{0}$ and $f_p = 0$. For the boundary conditions, we impose an

Table 1 The order of convergence of the velocity and the pressure in the L^2- and H^1- norm for Example 1. N is the number of mesh points.

Part	Field	Norm	$N = 13,810$	$N = 98,248$	$N = 741,373$
Stokes	Velocity ($\boldsymbol{u}_f$)	L^2	5.314×10^{-5}	1.428×10^{-5}	3.686×10^{-6}
		Order	-	1.896	1.954
		H^1	6.31×10^{-3}	3.27×10^{-3}	1.64×10^{-3}
		Order	-	0.948	0.989
	Pressure (p_f)	L^2	3.13×10^{-2}	8.19×10^{-3}	1.53×10^{-3}
		Order	-	1.936	2.418
		H^1	0.2623	0.2012	0.148
		Order	-	0.383	0.44
Darcy	Pressure (p_p)	L^2	1.79×10^{-3}	4.54×10^{-4}	1.14×10^{-4}
		Order	-	1.985	1.989
		H^1	0.04	0.02	0.01
		Order	-	1	1

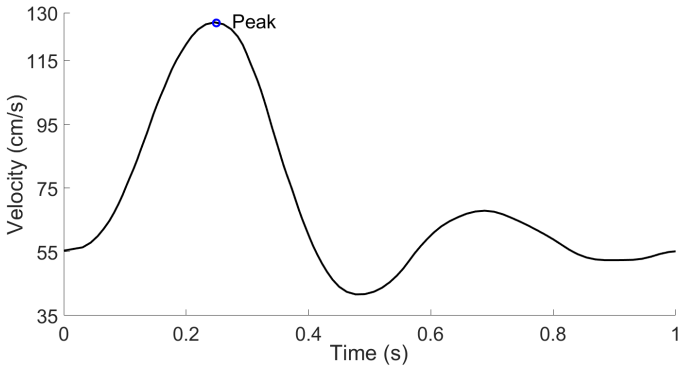

Figure 6 The pulsatile inflow velocity profile in a cardiac cycle with the peak systole $t = 0.24$ s labeled with a blue circle.

inflow pulsatile velocity profile[9] in a cardiac cycle shown in Fig. 6 on the inlet and a constant physiological venous pressure of 10 mmHg on the outlet. For the blood flow parameters, we set the density $\rho = 1.0$ g/cm^3 and the dynamic viscosity $\mu = 0.035$ g/(cm·s). Note that the ranges of the storativity S_0 and permeability k are generally $10^{-7} \sim 10^{-3}$ cm·s^2/g according to[50], and $10^{-8} \sim 10^{-6}$ cm$^3 \cdot$ s/g reported in[51,52], respectively. In this case, we set the storativity $S_0 = 10^{-3}$ cm·s^2/g and the permeability $k = 8 \times 10^{-6}$ cm^3·s/g such that the resulting pressures are within the range of typical values. In this case, we set the time step size $\Delta t = 0.02$ and use a mesh with 741,373 mesh points for the simulations.

First, Fig. 7 presents the distributions of the velocity and pressure at the peak systole. We observe in Fig. 7a that the velocity value is higher in the artery than that in the vein due to the pulsatile flow in the artery. In Fig. 7b, we can see that the systolic pressure reaches 120 mmHg at the inlet of the artery and 14 mmHg near the interface of the vein, and drops gradually from proximal to distal with an obvious pressure gradient in the artery and also a slight decrease in the vein. In the porous medium, a significant pressure change near the interface of the artery can be found in Fig. 7c, compared with that of the vein. In Fig. 8, we further show the local hemodynamic features and the velocity is largest near the wall and the corresponding pressure becomes smallest, as the fluid with higher velocity at the center of the artery, upon approaching the interface, flows toward the boundary of the interface due to the resistance of the porous medium.

To study the impact of the storativity S_0 and permeability k on the pressure, we monitor the change of the pressure with different settings of S_0 and k in the third cardiac cycle at four points P1, P2, P3 and P4 (see Fig. 5). We notice in Fig. 9 that for a fixed storativity, the pressure in the artery increases significantly as the permeability k decreases from 2×10^{-5}, 10^{-5} to 8×10^{-6}

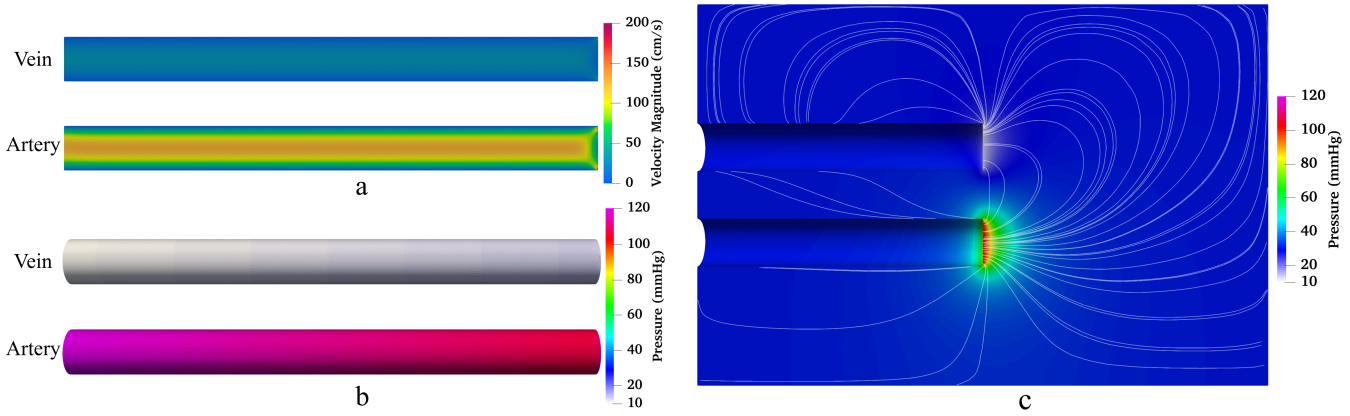

Figure 7 The results of numerical simulations at the peak systole $t = 0.24$ s for Example 2. (a) the distributions of the velocity magnitude in an axis section of the renal artery and vein. (b) The pressure distribution in the whole renal artery and vein. (c) The pressure and streamlines in an axial section of the kidney.

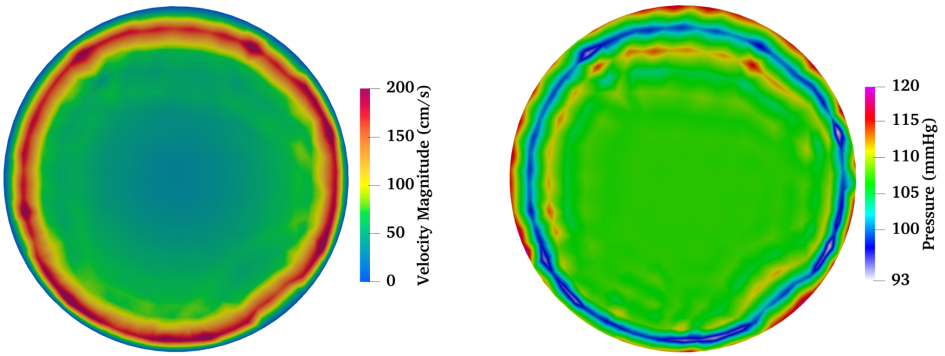

Figure 8 Velocity and pressure distributions on the interface of the artery at the peak systole for Example 2.

$cm^3 \cdot s/g$. When the permeability k is fixed, the decrease in the value of storativity leads to a slight increase in the pressure. We also observe a common phenomenon that the pressure is pulsatile in the artery and stable in the vein for all the tests.

Next we focus on the performance of the proposed preconditioner in terms of the number of iterations. Table 2 presents the number of iterations of different preconditioners with different meshes and ILU fill-in levels. As the mesh is refined, the system is harder to solve and the number of iterations increases. For a fixed mesh, the performance of the preconditioners is improved with the increase of the fill-in level from 1 to 2. In all cases, we observe that the two-level preconditioners can effectively improve the convergence of the one-level preconditioner and the 1D-0D and 1D-3D coarse preconditioners with ILU(2) perform quite well. In Table 3, we further study the impact of the viscosity μ, the storativity S_0 and the permeability k on the preconditioners. It can be seen that the one-level method doesn't work at all, the two-level methods work, but the 1D-3D coarse solver works much better.

5.3 | Example 3: A patient-specific kidney

The third example is to simulate blood flows in a realistic renal artery, renal vein and the kidney tissue. We adopt the same settings as in Example 2 for the boundary conditions and the parameters except for the storativity and the permeability which are set to $S_0 = 10^{-8}$ $cm \cdot s^2/g$ and $k = 4 \times 10^{-5}$ $cm^3 \cdot s/g$ in this case. We use a mesh with 488,047 mesh points and the time step size $\Delta t = 0.01$.

In Figs. 10 and 11, we show the simulation results including the distributions of the pressure and the velocity magnitude, as well as some local features at the peak systole $t = 0.24$ s. We clearly see that the pressure decreases from the inlet to the interface of the artery and the values are higher than those in the vein where the pressure is close to a constant value of 10 mmHg, which

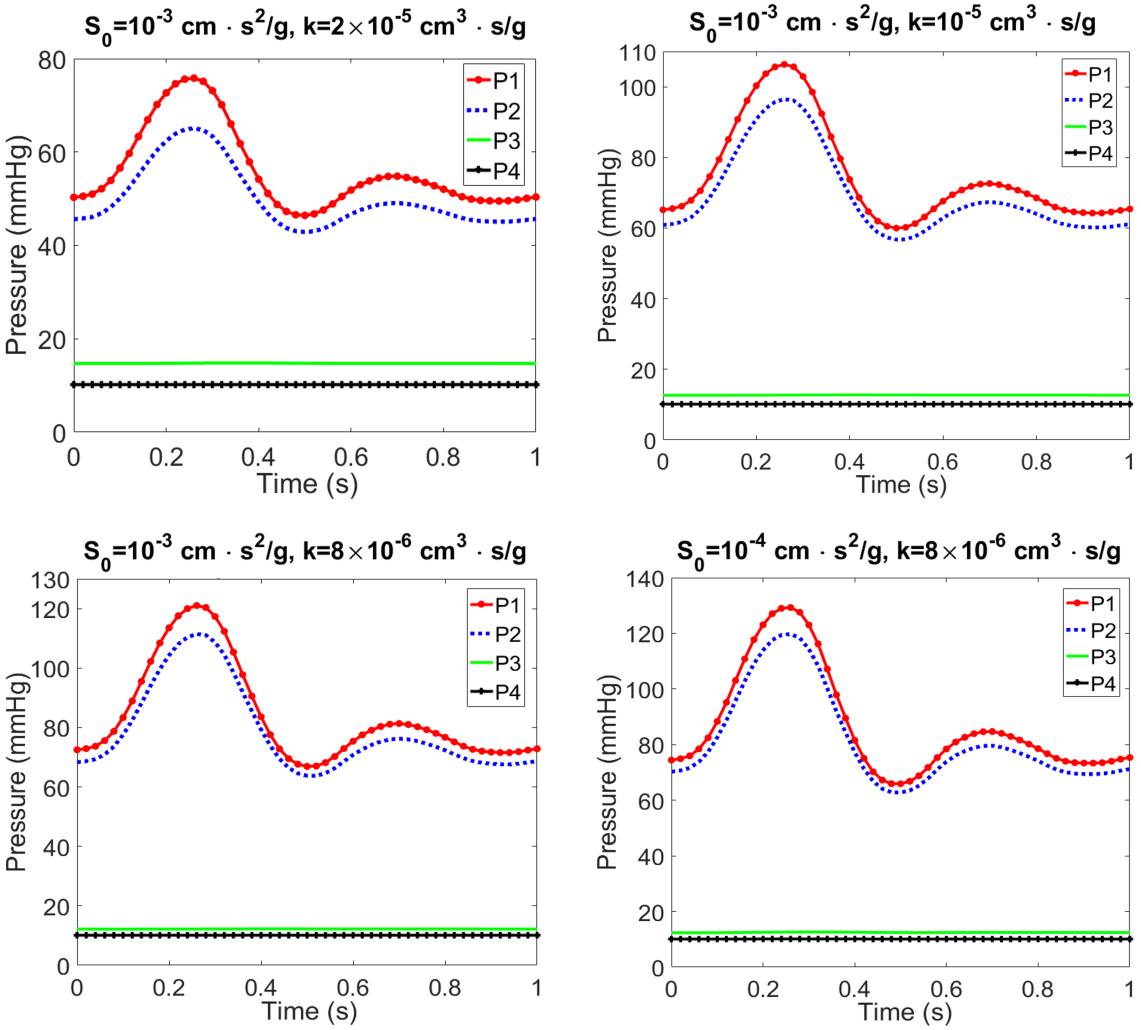

Figure 9 The changes of the pressure at four different points P1, P2, P3 and P4 in Fig. 5 for different storativities S_0 and permeabilities k in the third cardiac cycle for Example 2.

Table 2 The impact of the mesh size and fill-in level of the subdomain solvers ILU on the preconditioners in terms of the number of iterations for Example 2. '-' represents the value over the maximum allowed number of iterations.

Mesh	*np*	ILU	One-level	Two-level		
				0D	1D-0D	1D-3D
98,248	128	1	554	123	62	56
		2	290	91	41	37
741,373	512	1	-	270	147	138
		2	-	199	90	86

is similar to the results in Example 2. For the kidney tissue in Fig. 11, a noticeable pressure gradient near the interface can be observed and the gradual pressure distribution within the kidney tissue reflects the perfusion process, which is consistent with physiological observations. Following the streamlines, there is a significant pressure variation that facilitates the blood flow from the arteries to the kidney tissue and its subsequent return primarily through the veins that are adjacent to the corresponding arteries. This numerically computed perfusion process is similar to what is expected under the physiological conditions. Note

Table 3 The impact of the storativity S_0 and the permeability k on the preconditioners with ILU(2) in terms of the number of iterations for Example 2. '-' represents the value over the maximum allowed number of iterations.

Mesh	np	μ (g/cm·s)	S_0 (cm·s^2/g)	k (cm^3·s/g)	One-level	Two-level		
						0D	1D-0D	1D-3D
741,373	512	0.035	10^{-3}	10^{-3}	-	265	79	72
				10^{-6}	-	182	89	79
			10^{-6}	10^{-3}	-	231	75	71
				10^{-6}	-	199	96	82
		0.06	10^{-3}	10^{-3}	-	209	78	67
				10^{-6}	-	158	84	75
			10^{-6}	10^{-3}	-	192	74	67
				10^{-6}	-	173	91	78

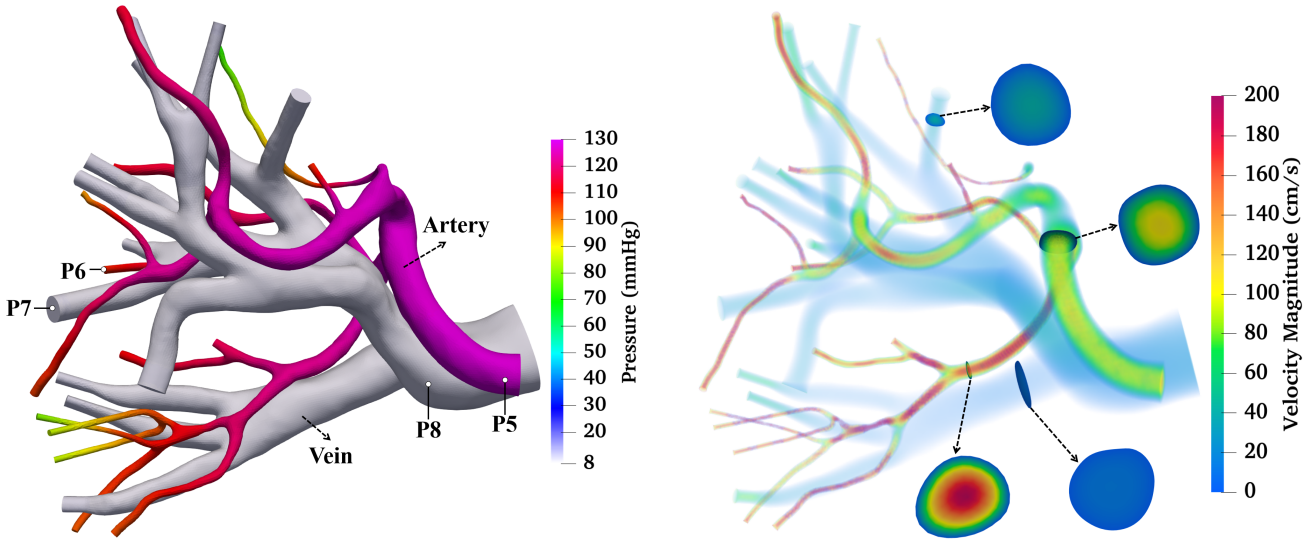

Figure 10 The pressure distribution and volume rendering of velocity magnitude in the renal artery and vein and local hemodynamics in four cross sections. Four points P5, P6, P7 and P8 are chosen to monitor the temporal changes of the pressure for Example 3.

that the zoom-in view of Fig. 11 shows that the blood perfusion for any region in the kidney is provided by multiple branches of the artery in order to maintain a stable blood supply. This phenomenon is likely associated with the collateral circulation that plays an important role particularly in the case of renal artery stenosis[53]. In Fig. 12, we also plot the variations of the pressure in the third cardiac cycle at eight different points shown in Fig. 10 and 11. A phenomenon, similarly observed in Example 2, can be seen that the pressures in the artery and the kidney tissue are pulsatile but the pressure in the renal vein changes very little.

Further for the realistic case, in Table 4, we consider the impact of the mesh size, the overlapping parameter δ and the ILU fill-in level on the performance of the preconditioners. We can see that the 1D-3D coarse preconditioner offers the optimal performance for both meshes, and ILU(2) greatly reduces the number of GMRES iterations, which is similar to the above results. For a fixed mesh and ILU fill-in level, the number of GMRES iterations almost decreases as δ increases from 0 to 2.

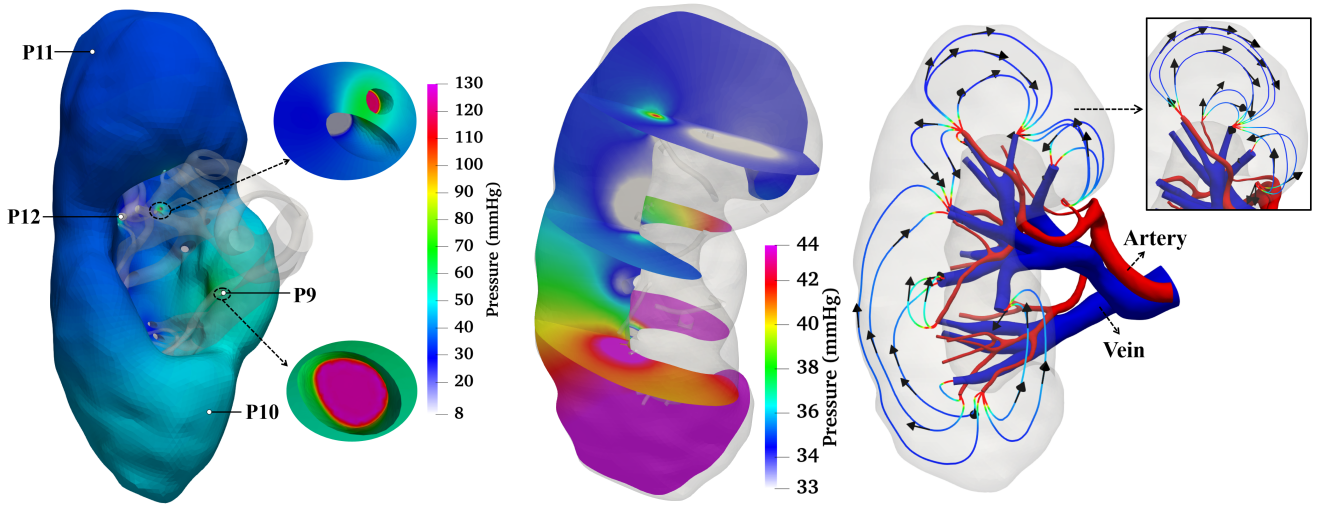

Figure 11 Pressure and streamline distributions in the kidney with zoom-in views and local pressure features in four cross sections, as well as four monitoring points P9, P10, P11 and P12 for Example 3.

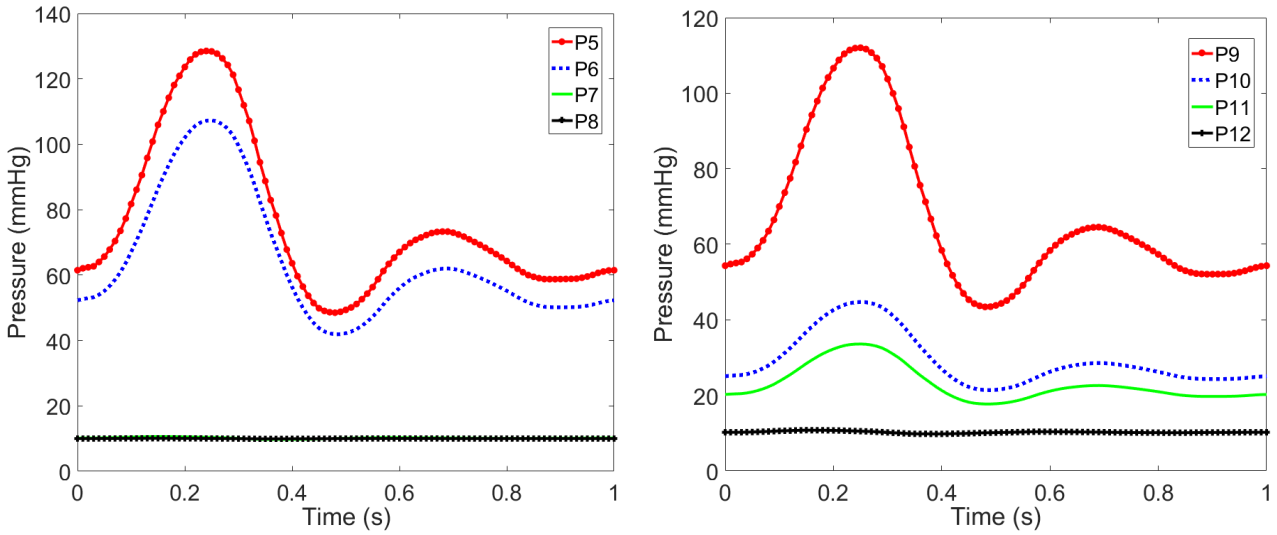

Figure 12 The changes of the pressure in the third cardiac cycle at 8 different points for Example 3.

5.4 | Example 4: A patient-specific kidney with additional wall boundary conditions between the artery/vein and the tissue

In Example 3, the interface region is selected as the distal outlets of the renal vessels and the vessel wells are considered non-penetrating. In this example, we assume that the interface region includes both the distal outlets and the vascular wall inside the kidney tissue. In other words, we assume a certain amount of flow penetrates the wall and this assumption simulates the tiny vessels that are not visible from the MRI images. Fig. 13 shows the computed distributions of the velocity and pressure in the renal vessels and kidney at the peak systole. Compared with these results in Example 3, the lower values of the pressure in the renal vessel and kidney can be observed due to an increase in the interface region. This makes sense because the vessels inside the kidney can be treated as a network of microvasculature whose wall serves as the interface facilitating blood perfusion which leads to a lower pressure than that in Example 3 where the wall inside the kidney is assumed to be impermeable. Generally speaking, the pressure value changes following the change of the permeability, more specifically, a smaller permeability may lead to larger pressure values, which can similarly be found in[54] for the hypertension case due to the microvascular rarefaction. Moreover, we also present the velocity magnitude in the renal vessels and the streamlines of cross sections of the artery and

Table 4 The impact of the subdomain solver and the overlapping size and the comparison of different Schwarz preconditioners in terms of the number of GMRES iterations with two meshes for Example 3. '-' represents the value over the maximum allowed number of iterations.

Mesh	*np*	ILU	δ	One-level	Two-level		
					0D	1D-0D	1D-3D
488,047	256	1	0	-	-	338	217
			1	-	-	308	281
			2	-	-	292	282
		2	0	-	350	136	81
			1	-	230	76	76
			2	-	290	114	75
1,515,564	1024	1	0	-	-	-	443
			1	-	-	340	217
			2	-	-	290	195
		2	0	-	361	187	103
			1	-	332	150	89
			2	-	344	141	87

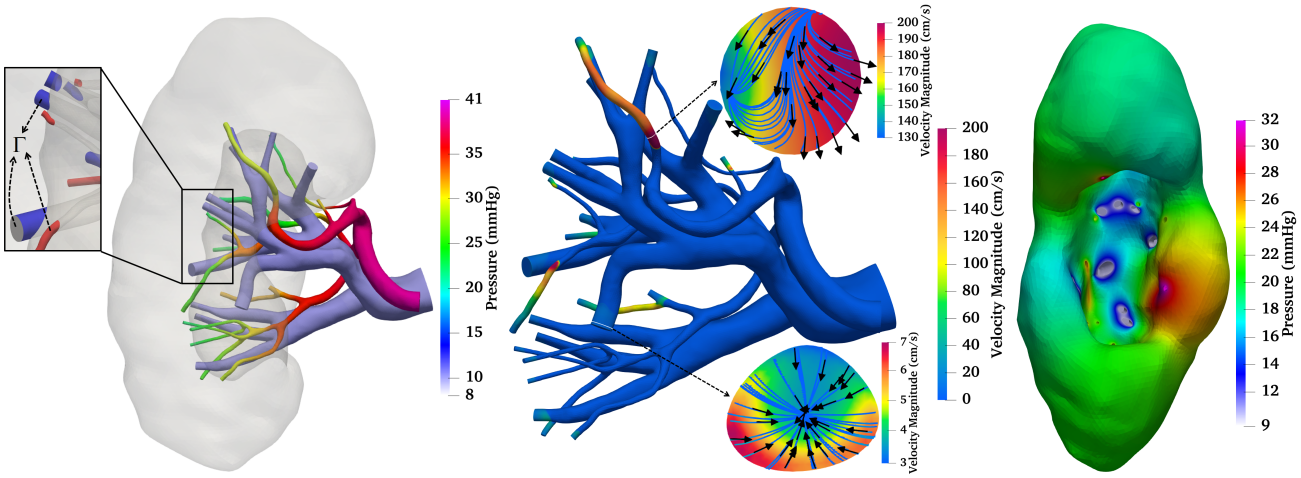

Figure 13 Distributions of the pressure and the velocity magnitude in renal vessels and the pressure distribution in the kidney at the peak systole for Example 4.

vein inside the kidney, which shows that the fluid can penetrate into the kidney across the part of the arterial wall in the kidney and collect in the vein.

To understand the performance of the iterative solver, in Table 5, we show the number of iterations with different preconditioners and the proposed preconditioner works better than other preconditioners for all cases. Compared with Table 4, the number of iterations for the 1D-3D preconditioner with ILU(2) has an obvious increase when the number of mesh points goes up to 1,515,564. In fact, the permeable vascular wall within the kidney tissue results in complex flow patterns in the vascular region, as shown in Figure 13. Consequently, the central-line coarse basis functions (28) and (30) defined in this region are less effective. Replacing them with radial coarse basis functions (32) fixes this issue. Fig. 14 plots the residual histories for Examples 3 and 4. It shows that the two-level methods significantly improve the convergence of the one-level method that converges quickly in the first few iterations but slowly in the later steps. Note that the proposed preconditioner is the best in terms of the number of iterations compared with others for both cases.

Table 5 The number of GMRES iterations for different number of subdomains with two meshes for Example 4. '-' represents the value over the maximum allowed number of iterations.

Mesh	*np*	ILU	One-level	Two-level		
				0D	1D-0D	1D-3D
488,047	256	1	-	393	195	179
		2	-	399	130	88
	512	1	-	360	191	155
		2	-	269	127	88
1,515,564	512	1	-	-	-	195
		2	-	427	192	134
	1024	1	-	-	372	370
		2	-	397	197	162

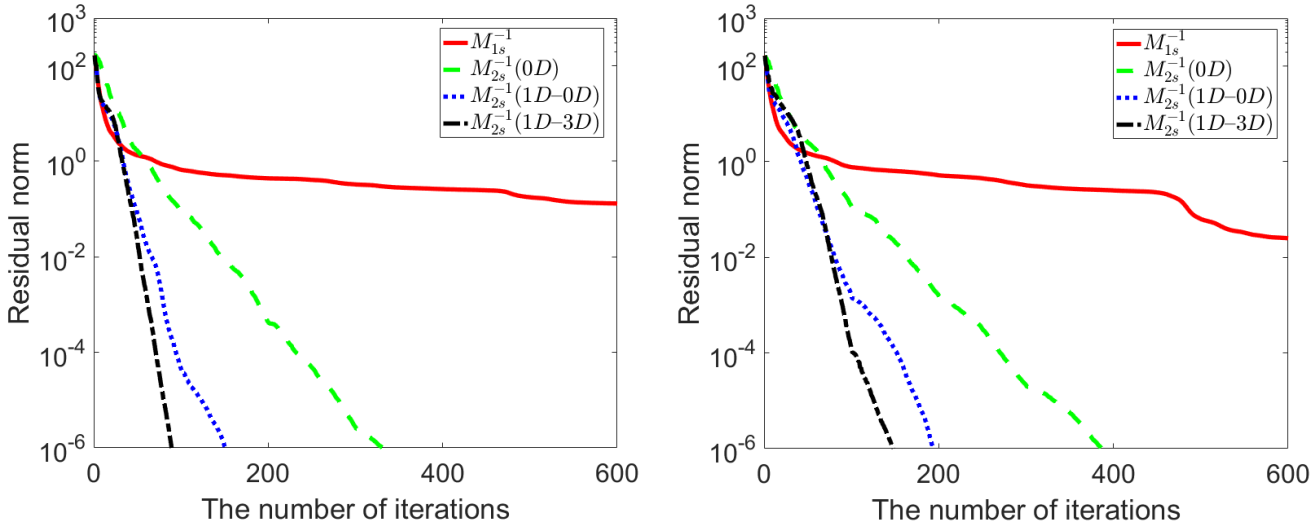

Figure 14 The number of iterations of different preconditioners for Example 3 (left) and 4 (right) based on the mesh with 1,515,564 mesh points and 1024 subdomains and the ILU(2) subdomain solver.

6 | CONCLUSIONS

In this paper, we develop a coupled unsteady Stokes-Darcy system to model the blood flow in the patient-specific renal artery, vein and kidney tissue. Several interface conditions between the blood vessels and the kidney tissue are considered to model the penetration of the arterial wall and the perfusion of the kidney. To numerically simulate the behavior of the blood flow, a stabilized finite element method and the implicit backward Euler method are employed and the corresponding discretized systems are solved by a preconditioned Krylov subspace method. A stability theory is established for the discrete inf-sup condition and the convergence of the implicit finite element method is also proved in a parameter dependent norm. The convergence and order of convergence are verified numerically for some test cases. Moreover, we introduce an efficient two-level additive Schwarz preconditioner to accelerate the convergence of the Krylov solver. The key component of the preconditioner is a multi-scale coarse preconditioner consisting of a one-dimensional central-line coarse preconditioner and a three-dimensional coarse preconditioner through some suitable coarse-fine grids interpolation and extension operators. Note that the linear Stokes equations are considered in the vascular region and an isotropic and homogeneous permeability is assumed in the numerical simulation. The focus of the paper is on the development of the numerical methods, in the future work, a more realistic nonlinear model will be considered to bring the work closer to actual clinical applications.

ACKNOWLEDGEMENTS

The research was supported by the NSFC Grant 12201658, the Macau FDCT Grant 0084/2023/ITP2, 0146/2024/RIA2, 0079/2021/AFJ, and 0141/2020/A3.

ETHICAL STATEMENT

Not applicable.

CONFLICT OF INTEREST STATEMENT

The authors declare no conflicts of interest.

DATA AVAILABILITY STATEMENT

The data that support the findings of this study are available from the corresponding author upon reasonable request.

References

1. Subramanian R, White CJ, Rosenfield K, et al. Renal fractional flow reserve: a hemodynamic evaluation of moderate renal artery stenoses. *Catheter. Cardiovasc. Interv.* 2005; 64(4): 480–486.

2. Mikelic A, Jäger W. On the interface boundary condition of Beavers, Joseph, and Saffman. *SIAM J. Appl. Math.* 2000; 60(4): 1111–1127.

3. Discacciati M, Miglio E, Quarteroni A. Mathematical and numerical models for coupling surface and groundwater flows. *Appl. Numer. Math.* 2002; 43(1-2): 57–74.

4. Hanspal N, Waghode A, Nassehi V, Wakeman R. Numerical analysis of coupled Stokes/Darcy flows in industrial filtrations. *Transp. Porous Media* 2006; 64: 73–101.

5. Arbogast T, Lehr HL. Homogenization of a Darcy–Stokes system modeling vuggy porous media. *Comput. Geosci.* 2006; 10: 291–302.

6. Qin S, Wu B, Liu J, et al. Numerical simulation of blood flows in patient-specific abdominal aorta with primary organs. *Biomech. Model. Mechanobiol.* 2021; 20: 909-924.

7. Chen R, Wu B, Cheng Z, et al. A parallel non-nested two-level domain decomposition method for simulating blood flows in cerebral artery of stroke patient. *Int. J. Numer. Methods Biomed. Eng.* 2020; 36(11): e3392.

8. Quarteroni A, Manzoni A, Vergara C. The cardiovascular system: mathematical modelling, numerical algorithms and clinical applications. *Acta Numer.* 2017; 26: 365–590.

9. Taylor CA, Hughes TJ, Zarins CK. Finite element modeling of three-dimensional pulsatile flow in the abdominal aorta: relevance to atherosclerosis. *Ann. Biomed. Eng.* 1998; 26: 975–987.

10. Berg N, Fuchs L, Prahl Wittberg L. Blood flow simulations of the renal arteries – effect of segmentation and stenosis removal. *Flow Turbul. Combust.* 2019; 102: 27–41.

11. Deng W, Tsubota Ki. Numerical simulation of the vascular structure dependence of blood flow in the kidney. *Med. Eng. Phys.* 2022; 104: 103809.

12. Bortolussi C. Computational modeling of flow in the kidney. 2018.

13. Hou J, Qiu M, He X, Guo C, Wei M, Bai B. A dual-porosity-Stokes model and finite element method for coupling dual-porosity flow and free flow. *SIAM J. Sci. Comput.* 2016; 38(5): B710–B739.

14. Stoter SK, Müller P, Cicalese L, Tuveri M, Schillinger D, Hughes TJ. A diffuse interface method for the Navier–Stokes/Darcy equations: Perfusion profile for a patient-specific human liver based on MRI scans. *Comput. Methods Appl. Mech. Engrg.* 2017; 321: 70–102.

15. Rohan E, Lukeš V, Jonášová A. Modeling of the contrast-enhanced perfusion test in liver based on the multi-compartment flow in porous media. *J. Math. Biol.* 2018; 77(2): 421–454.

16. Di Gregorio S, Fedele M, Pontone G, et al. A computational model applied to myocardial perfusion in the human heart: from large coronaries to microvasculature. *J. Comput. Phys.* 2021; 424: 109836.

17. Rui H, Zhang R. A unified stabilized mixed finite element method for coupling Stokes and Darcy flows. *Comput. Methods Appl. Mech. Engrg.* 2009; 198(33-36): 2692–2699.

18. Badea L, Discacciati M, Quarteroni A. Numerical analysis of the Navier–Stokes/Darcy coupling. *Numer. Math.* 2010; 115: 195–227.

19. Cao Y, Gunzburger M, Hu X, Hua F, Wang X, Zhao W. Finite element approximations for Stokes–Darcy flow with Beavers–Joseph interface conditions. *SIAM J. Numer. Anal.* 2010; 47(6): 4239–4256.

20. Kanschat G, Riviere B. A strongly conservative finite element method for the coupling of Stokes and Darcy flow. *J. Comput. Phys.* 2010; 229(17): 5933–5943.

21. Layton WJ, Schieweck F, Yotov I. Coupling fluid flow with porous media flow. *SIAM J. Numer. Anal.* 2002; 40(6): 2195–2218.

22. Gatica GN, Meddahi S, Oyarzúa R. A conforming mixed finite-element method for the coupling of fluid flow with porous media flow. *IMA J. Numer. Anal.* 2009; 29(1): 86–108.

23. Ervin V, Jenkins EW, Sun S. Coupled generalized nonlinear Stokes flow with flow through a porous medium. *SIAM J. Numer. Anal.* 2009; 47(2): 929–952.

24. Mu M, Zhu X. Decoupled schemes for a non-stationary mixed Stokes-Darcy model. *Math. Comp.* 2010; 79(270): 707–731.

25. Discacciati M, Oyarzúa R. A conforming mixed finite element method for the Navier–Stokes/Darcy coupled problem. *Numer. Math.* 2017; 135(2): 571–606.

26. Girault V, Rivière B. DG approximation of coupled Navier–Stokes and Darcy equations by Beaver–Joseph–Saffman interface condition. *SIAM J. Numer. Anal.* 2009; 47(3): 2052–2089.

27. Lipnikov K, Vassilev D, Yotov I. Discontinuous Galerkin and mimetic finite difference methods for coupled Stokes–Darcy flows on polygonal and polyhedral grids. *Numer. Math.* 2014; 126(2): 321–360.

28. Tlupova S, Cortez R. Boundary integral solutions of coupled Stokes and Darcy flows. *J. Comput. Phys.* 2009; 228(1): 158–179.

29. Cai M, Mu M, Xu J. Numerical solution to a mixed Navier–Stokes/Darcy model by the two-grid approach. *SIAM J. Numer. Anal.* 2009; 47(5): 3325–3338.

30. Discacciati M, Quarteroni A, Valli A. Robin–Robin domain decomposition methods for the Stokes–Darcy coupling. *SIAM J. Numer. Anal.* 2007; 45(3): 1246–1268.

31. Chen W, Gunzburger M, Hua F, Wang X. A parallel Robin–Robin domain decomposition method for the Stokes–Darcy system. *SIAM J. Numer. Anal.* 2011; 49(3): 1064–1084.

32. Boubendir Y, Tlupova S. Domain decomposition methods for solving Stokes–Darcy problems with boundary integrals. *SIAM J. Sci. Comput.* 2013; 35(1): B82–B106.

33. Liu Y, He Y, Li X, He X. A novel convergence analysis of Robin–Robin domain decomposition method for Stokes–Darcy system with Beavers–Joseph interface condition. *Appl. Math. Lett.* 2021; 119: 107181.

34. Klawonn A, Rheinbach O. Highly scalable parallel domain decomposition methods with an application to biomechanics. *ZAMM · Z. Angew. Math. Mech.* 2010; 90(1): 5–32.

35. Discacciati M, Gerardo-Giorda L. Optimized Schwarz methods for the Stokes–Darcy coupling. *IMA J. Numer. Anal.* 2018; 38(4): 1959–1983.

36. Liu Y, Boubendir Y, He X, He Y. New Optimized Robin–Robin Domain Decomposition Methods using Krylov Solvers for the Stokes–Darcy System. *SIAM J. Sci. Comput.* 2022; 44(4): B1068–B1095.

37. Bochev PB, Gunzburger MD, Shadid JN. On inf–sup stabilized finite element methods for transient problems. *Comput. Methods Appl. Mech. Engrg.* 2004; 193(15-16): 1471–1489.

38. Brezzi F, Douglas J. Stabilized mixed methods for the Stokes problem. *Numer. Math.* 1988; 53: 225–235.

39. Badia S, Codina R. Unified stabilized finite element formulations for the Stokes and the Darcy problems. *SIAM J. Numer. Anal.* 2009; 47(3): 1971–2000.

40. Cao Y, Gunzburger M, Hua F, Wang X. Coupled Stokes-Darcy model with Beavers-Joseph interface boundary condition. *Commun. Math. Sci.* 2010; 8(1): 1–25.

41. Girault V, Raviart PA. *Finite Element Methods for Navier-Stokes Equations: Theory and Algorithms*. Springer-Verlag, Berlin . 1986.

42. Brenner SC. *The Mathematical Theory of Finite Element Methods*. Springer . 2008.

43. Cai XC, Sarkis M. A restricted additive Schwarz preconditioner for general sparse linear systems. *SIAM J. Sci. Comput.* 1999; 21(2): 792–797.

44. Liu Y, Qi F, Cai XC. An aneurysm-specific preconditioning technique for the acceleration of Newton-Krylov method with application in the simulation of blood flows. *Int. J. Numer. Methods Biomed. Eng.* 2023; 39(12): e3771.

45. Liu Y, Qi F, Cai XC. A one-dimensional coarse preconditioner for three-dimensional unsteady incompressible Navier-Stokes flows in patient-specific arteries. *SIAM J. Sci. Comput.* 2023; 46(2): S1–S23.

46. Liu Y, Cai XC. Two-level additive Schwarz methods for three-dimensional unsteady Stokes flows in patient-specific arteries with parameterized one-dimensional central-line coarse preconditioner. *J. Comput. Phys.* 2023; 490: 112290.

47. Wendland H. Piecewise polynomial, positive definite and compactly supported radial functions of minimal degree. *Adv. Comput. Math.* 1995; 4: 389–396.

48. Deparis S, Forti D, Quarteroni A. A rescaled localized radial basis function interpolation on non-Cartesian and nonconforming grids. *SIAM J. Sci. Comput.* 2014; 36(6): A2745–A2762.

49. Quarteroni A, Formaggia L. Mathematical modelling and numerical simulation of the cardiovascular system. *Handbook of Numerical Analysis* 2004; 12: 3–127.

50. Bear J. *Hydraulics of Groundwater*. Courier Corporation . 2012.

51. Liao Z, Poh CK, Huang Z, Hardy PA, Clark WR, Gao D. A numerical and experimental study of mass transfer in the artificial kidney. *J. Biomech. Eng.* 2003; 125(4): 472–480.

52. Deen WM, Lazzara MJ, Myers BD. Structural determinants of glomerular permeability. *Am. J. Physiol.-Renal Physiol.* 2001; 281(4): F579–F596.

53. Afarideh M, Zhang X, Ferguson CM, et al. Peristenotic collateral circulation in atherosclerotic renovascular disease: association with kidney function and response to treatment. *Hypertension* 2020; 76(2): 497–505.

54. Feihl F, Liaudet L, Waeber B, Levy BI. Hypertension: a disease of the microcirculation?. *Hypertension* 2006; 48(6): 1012–1017.